Modelling of liquid oxygen nozzle flows under subcritical and supercritical pressure conditions

T. Lyras[1,*], I.K. Karathanassis[1], N. Kyriazis[1], P. Koukouvinis[1] and M. Gavaises[1]
[1]School of Mathematics, Computer Science and Engineering, City, University of London, Northampton Square, EC1V 0HB, London, UK
[*]Corresponding author: Theodoros.Lyras.2@city.ac.uk

Abstract. The two-phase flow of liquid oxygen in a converging-diverging nozzle has been numerically predicted at conditions resembling those that prevail in the lower-stage boosters of rocket engines realising lift off, as well as in the respective upper stages operating in sub-atmospheric pressures. A comparative evaluation of the predictive capability of a pressure and a density-based solver with various approaches regarding the imposed phase-change rate and thermodynamics closure have been performed. The departure from thermodynamic equilibrium during phase-change has been taken into account via implementation of a bubble-dynamics model employing the Hertz-Knudsen equation in the pressure based solver, whereas thermodynamic equilibrium is adopted in the density-based solver. Tabulated data for the variation of the fluid thermodynamic properties have been derived by the Helmholtz Equation of State (EoS) in a modelling approach universal for both the sub- and supercritical states. This approach has been comparatively assessed in the sub-critical regime against the bubble-dynamics-based model including different EoS for the liquid/vapour phases and against a different tabulated approach based on the NIST dataset for supercritical injection. In terms of flow physics, more severe flow expansion in the diverging part of the nozzle has been detected for subcritical pressures, leading to supersonic flow velocities and significant cooling of the fluid mixture. Complementary Detached Eddy Simulations (DES) have provided detailed insight on the complex expansion phenomena and flow instabilities manifesting on the divergent part of the nozzle for subcritical-injection conditions. The comparison of the numerical predictions against available experimental data and analytical solutions demonstrates the suitability of the employed methodologies in describing the evolution of the cryogenic oxygen flow expansion and phase-change.

Key words: cryogenic LOx, rocket engine, real-fluid thermodynamics, flash boiling, compressible flow

Nomenclature

A	area (m^2)
a	molar Helmholtz energy (J)
α^0	dimensionless ideal gas contribution to the Helmholtz energy (-)
α^r	dimensionless residual Helmholtz energy (-)
c	speed of sound ($m\ s^{-1}$)
d	diameter (m)
e	internal energy ($J\ kg^{-1}$)
k	thermal conductivity ($W\ m^{-1}\ K^{-1}$)
M	Mach number (-), M=u/c
N	Finite element nodal shape function
$\dot{m}$	mass flow rate ($kg\ s^{-1}$)
L	length (m)
p	pressure (Pa)
R	specific gas constant ($J\ kg^{-1}\ K^{-1}$)
Re	Reynolds number (-)
R_g	ideal gas constant, R_g = 8.31446 ($J\ mol^{-1}\ K^{-1}$)
R_p	degree of superheat (-), $R_p=p_{sat}(T_{in})/p_{out}$

$\dot{R}$	phase-change rate kg m^{-3} s^{-1}
T	temperature (K)
t	time (s)
u	velocity (m s^{-1})

Greek Letters

α	volume fraction (-)
δ	dimensionless density (-)
λ	accommodation coefficient (-)
λ_g	Taylor length scale (m)
μ	viscosity (N s m^{-2})
ρ	density (kg m^{-3})
τ	dimensionless temperature (-)

Subscripts

c	critical
exp	experimental value
g	gas
in	inlet
int	interface
max	maximum
min	minimum
n	node number
out	outlet
sat	saturation
t	throat
v	vapour

1. Introduction

Liquid oxygen (LOx) constitutes a widely used propellant in multistage rockets for space launch vehicles. It is characterised as a cryogenic liquid as it remains in this state at temperatures below 90K. The combination of liquid hydrogen/oxygen, as the fuel/oxidiser propellants mixture has been employed in various launch vehicles developed from the 1960s up to now [1]. For instance, LOx/LH_2 propellants were burned in the main engines of the NASA Space Shuttle, the upper stages of the Ares I crew-launch vehicle, as well as the upper rocket stage (Centaur) of Atlas [2]. The same combination of propellants is also used by ESA in the upper stages of the Ariane 5 launch vehicles [3]. They have also been employed in the 2nd and 3rd stages of Saturn V, the 1st and 2nd stage and the upper stage of the family of Japanese H-II and Indian GSLV satellite-launch rockets, respectively. Modern commercial rockets such as the Falcon and BE-4 currently developed by SpaceX and Blue Origin, respectively, have adopted the use of LOx/LCH_4 as propellants. For lower-stage boosters realising lift-off and thus operating at atmospheric conditions, LOx is usually mixed with kerosene (RP-1), as e.g. in the cases of Saturn V, Atlas V, the Russian Soyuz, and SpaceX Falcon rockets.

It is essential to mention that the upper stages of rocket launch-vehicles are designed to operate at high altitude, where near-vacuum conditions ensue. As a general practice, these stages incorporate combustion chambers operating at lower pressures compared to the lower-stage counterparts [4]. Hence, depending on the specific rocket-engine design and its location at the tandem-stage configuration, the delivery of LOx to mix with the main fuel could be realised at either supercritical (lower-stages) or subcritical (upper stages) pressure conditions. For reference, the critical point for oxygen corresponds to 50.4 bar/154.6 K [5]. LOx phase change due to rapid pressure drop is expected to occur in the oxidiser-delivery nozzle, especially during engine start-up, where vacuum conditions may exist. The topology and dynamics of the compressible flow will be designated to a great extent by the steepness of the density gradient. In the case that the process evolves at subcritical pressures, the fluid density exhibits an abrupt change, as an interphase sets in between the liquid and vapour phases, i.e. bubbles form. The rapid bubble nucleation within the entire bulk of the liquid due to rapid depressurisation is characterised as flash boiling, a flow phenomenon that is possible to be encountered in cryogenic fluids [6], refrigerants [7] and light hydrocarbons [8]. On the contrary, for supercritical conditions, no interface emerges and the fluid density exhibits a smooth variation with pressure.

Experimental studies focusing on nozzle and spray flows of cryogenic oxygen for a wide range of flow conditions are relatively limited in the open literature due to the technical difficulties associated with the handling and storage of the substance at cryogenic temperatures and the extreme conditions that the experimental hardware must withstand, especially at supercritical pressures/temperatures [9]. The technical note of Hendricks et al. [10] is one of the early studies made available by NASA reporting measurements of the pressure distribution of two-phase LOx flow within a Venturi nozzle at subcritical pressures. Early studies by Mayer and co-workers [11], [12] utilised different optical methods to pinpoint the differences in topology of cryogenic-liquid jets being expelled at an environment of either sub- (of the order of 15 bar) or supercritical-pressure conditions (100 bar). The topology and degree of atomization of LOx sprays at 10 bars has also been investigated at the Mascotte test bench of ONERA [13]. Cherhoudi et al. [14] conducted backlit-illumination visualisation to illustrate the topology of LOx and LN_2 jets injected into a gaseous environment at conditions ranging from sub- to supercritical pressures and supercritical temperatures. Quantitative data regarding the jet cone angle were obtained and it was verified that the jet growth rate measurements were in agreement with the theoretical predictions for gaseous jets of variable density. More recently, the shadowgraphy visualisation conducted by Lamanna et al. [15] considering subcritical LOx and ethanol sprays at injection pressures up to 17 bar demonstrated that a higher degree of superheat is required for the inception of flash boiling in cryogenic compared to storable propellants. According to the nucleation theory proposed by the same authors in [16], this is due to the higher surface energy work at low temperatures, which must be surpassed by the fluid chemical potential, in order vapour bubbles to form.

It can be therefore deducted that, due to the complexities associated with experimental campaigns, accurate numerical modelling is crucial for cryogenic-propellant flow applications. At supercritical pressures, the suitability of the modelling approach is highly dependent on the selection of an Equation of State capable to capture the thermodynamic properties of the fluid at very high pressures and temperatures. A number of studies available in the literature refer to supercritical injection or expanding-nozzle flow of refrigerants like liquid CO_2. Thermodynamic closure is commonly accomplished through the use of cubic equations of state [17]–[20]. It has been verified that the selection of EoS (i.e. Peng-Robinson (PR), Benedict-Webb-Rubin, Span-Wagner) has a considerable impact on the numerical prediction of supersonic CO_2 accelerating flows, as it affects the location and intensity of emerging shockwave patterns [21].

With reference to cryogenic fluids, research on supercritical injection is mainly focused on liquid nitrogen or oxygen as working media. Different sub-grid scale (SGS) models for LES along with volume translation methods for the PR were comparatively evaluated by Müller et al. [22] with regards to liquid nitrogen injection. It was found that the effect of thermodynamics modelling was more profound for the case of transcritical compared to supercritical injection, while the selection of SGS model only had a minor influence on temporal evolution of the jet mean density. Poormahmoud et al. [23] investigated the dispersion dynamics of LN_2 inside and downstream the outlet of a single-orifice swirl atomiser. The SST k-ω and the SRK EoS were employed for turbulence and thermodynamic closure, respectively. The pattern of vortical structures emerging at the diverging part of the flow layout was illustrated along with their transient features. Kang et al. [24] conducted a similar study using the same EoS in a LES framework. Apart from hydrodynamic instabilities, the study also highlighted the acoustic instabilities affecting the flow field. Likewise, supercritical LOx injection has been mainly investigated numerically with reference to swirl atomisers suitable for rocket engines. Zong et al. [25] performed an LES study referring to a LOx swirl injector using the Soave-Redlich-Kwong (SRK) and Benedict–Webb–Robin EoSs for the calculation of the fluid thermodynamic and transport properties, respectively. Kelvin–Helmholtz instabilities were demonstrated to be the primary cause leading to supercritical mixing. Wang et al. [26] employed the modified SRK EoS to describe the thermodynamic properties of LOx during supercritical injection, while in a subsequent study [27] the same approach was followed to illustrate the LOx/kerosene mixing characteristics. Both studies focused on the influence of hydrodynamic instabilities on the propellants dispersion in the expanding geometry downstream the injector outlet.

Concerning subcritical conditions, jet atomization and the formation of a two-phase spray is the process governing the combustion behaviour of the oxidizer/fuel mixture. In the case that flash-boiling conditions are met, the oxidiser rapid vaporisation within the injector orifice has a tremendous influence on the characteristics of the expelled spray. Studies on water, refrigerants and light hydrocarbons have demonstrated that in nozzle-flash boiling leads to the production of finer sprays with higher cone angles and reduced penetration lengths compared to nozzle flows with inertia-driven phase change (i.e. cavitation) [28]. Nevertheless, few numerical studies have been found in the open literature illustrating the distinct features of cryogenic-liquid is et al. [29] developed a theoretical two-phase model based on the Helmholtz energy EoS capable of predicting the critical flow rate for choked flows of cryogenic fluids. A correction on the homogeneous equilibrium model was implemented to take into account non-equilibrium effects. The theoretical predictions for different cryogenic liquids were found to be in good agreement with experimental results for the critical flow rate. Lyras et al. [30] employed the Homogeneous Relaxation Model coupled to the volume-of-fluid method to predict the flashing phase-change in a throttle nozzle and subsequent spray expansion of liquid nitrogen. Schmehl and Steelant [31] used an Eulerian-Lagrangian frame to simulate the pre-flow of di-nitrogen tetroxide (N_2O_4) oxidiser in a co-axial flow injector considering a dilute mixture of liquid droplets and vapour. Droplet flash vaporisation was described through an empirical model based on pre-existing measurements. A similar numerical approach was adopted by Ramcke et al. [32] to simulate the spray dynamics of LOx pre-flow and the mixing behaviour of the oxidiser with gaseous methane. Both studies concur that cryogenic flashing sprays exhibit the same distinct features as those of storable liquids, namely enhanced droplet atomisation, increased cone angle and

acceleration of the compressible mixture. Gaillard et al. [33] employed two coupled-flow solvers to perform LES of LOx spray atomisation with relevance to the experiments performed at ONERA [13]. The gaseous and dispersed phases were treated in an Eulerian framework, while the Abramzon-Sirignano [34] model was used for evaporation and heat transfer.

The outlined literature overview makes clear that different modelling approaches have been implemented to predict cryogenic-liquid injection in an ad-hoc manner, primarily depending on the thermodynamic regime and specific flow features, e.g. swirling flows. To the authors' knowledge this is the first work in the open literature to propose and evaluate a modelling framework suitable for the prediction of multiphase, cryogenic wall-bounded flows for a wide range of pressure conditions and capable of reproducing distinct features such as flash vaporisation, supersonic expansion and transition to a supercritical state. The present study constitutes a comparative investigation on the predictive accuracy of different methods regarding in-nozzle phase-change in both sub- and supercritical regimes. Furthermore, a universal methodology based on tabulated thermodynamics applicable to both regimes is demonstrated. Previous works of the authors' group ([35],[36]) have demonstrated the robustness of the technique in modelling phase change and spray mixing in fuel-injection applications. The tabulation technique has been extended to cryogenic oxygen in this work, based on the Helmholtz energy EoS for the calculation of thermodynamic properties. Unlike the majority of available studies, the present work focuses mainly on the in-nozzle, compressibility related, flow phenomena and highlights their influence on the spray expansion and dynamics. Further to the URANS simulations performed, hydrodynamic-instability effects have been assessed through DES.

2. Numerical methodology

Two flow solvers, an implicit coupled pressure/velocity and an explicit density-based, have been employed in the present investigation. The basic set of governing equations solved in both cases comprised the continuity, momentum and energy conservation equations. The complete formulations of the adopted numerical methodologies, along with the sets of equations solved are described in detail by Karathanassis et al. [37] and Kyriazis et al. [38], [39] respectively, with reference to the pressure- and density -based solvers discussed in the following sections.

2.1 Pressure-based solver

Referring to the subcritical regime, a two-phase mixture approach was implemented in the coupled solver including an additional equation for the vapour transport. On the contrary, a single-fluid approach was adopted for the simulations in the supercritical regime, where the fluid properties for each computational cell were provided by the REFPROP dataset. Numerical schemes with second-order accuracy were employed for the discretisation of the governing equations. The QUICK scheme was employed for the discretisation of the vapour-fraction equation, while a second-order upwind scheme was used for density interpolation, as well as for the discretisation of the momentum and turbulence transport equations. An implicit, second-order backward differencing technique was used for time integration with a time-step value of 10^{-6} s, resulting to a CFL criterion value less than 1 in the entire domain for the DES cases examined.

A bubble-dynamics based model was employed in the coupled solver to capture the phase-change process under subcritical conditions. Mechanical equilibrium, i.e. a common velocity field, was also assumed for the two phases. Liquid LOx compressibility was imposed through the Tait EoS, while the respective vapour phase was treated as an ideal gas. The set of governing equations for the mixture was complemented by an advection equation for the conservation of the vapour phase volume fraction as follows:

$$\frac{\partial(a_v\,\rho_v)}{\partial t} + \nabla(a_v\,\rho_v\vec{u}) = \dot{R} \tag{1}$$

where the phase-change rate $\dot{R}$ corresponds to that of flash vaporisation. For the simulations of this study, the rate was calculated from the Hertz-Knudsen equation derived from kinetic theory of gases [40]:

$$\dot{R} = \frac{\lambda A_{int} (p_{sat} - p)}{\sqrt{2 \pi R_g T_{int}}} \tag{2}$$

where R_g and T_{int} are the ideal-gas constant and the bubble-interphase temperature respectively, while A_{int} is the overall vapour interface surface area, calculated as in [37]. Since a mixture model is employed, the interphase temperature is taken as equal to the local grid cell temperature provided by the solution of the energy equation. The degree of deviation from thermodynamic-equilibrium is reflected on the value of the accommodation coefficient λ. Values of either 1.0 or 0.1 correspond to conditions similar to thermodynamic-equilibrium and strongly deviating from it, respectively [41]. The capability of the Hertz-Knudsen model in capturing the phase-change rate with reference to flashing flows has been demonstrated in [37]. The model has also been utilised to describe phase-change in both fundamental bubble-dynamics studies [40] and more applied simulations with reference to gasoline fuel injectors [42]. This work demonstrates its applicability with reference to in-nozzle cryogenic flows.

The refrigerants and refrigerant-mixtures database (REFPROP v.9.1) of the National Institute of Standards and Technology (NIST) contains thermodynamic and transport properties for oxygen; the properties provided by REFPROP have been derived using the Helmholtz energy EoS, as described by Schmidt and Wagner in [43]. Further details on the EoS used for the derivation of the fluids properties can be found in [44], [45]. For test cases corresponding to supercritical pressures, the REFPROP library is dynamically loaded into the coupled solver in the form of a pre-formulated look-up (structured) matrix. Material properties are stored in the matrix as a function of local pressure and temperature. For the present simulations a 201×201 matrix has been formulated with pressure and temperature lying within the ranges 500.0 kPa≤p≤15.5 MPa and 56.0 K≤T≤156.0 K, respectively.

2.2 Density-based solver

The 3-D RANS equations in conservative form were considered in the density-based solver, where a single-fluid modelling approach has been formulated in both the sub- and supercritical regimes. In essence, referring to the subcritical regime, an infinite phase-change rate was assumed at the bubble interface, i.e. establishment of thermodynamic equilibrium, and the entire process was replicated by an appropriate EoS. Since the Mach number is plausible to obtain a wide range of values in the simulated cases, owing to the fluid phase transitions (pure liquid, vapour, two-phase mixture or supercritical fluid), a Mach-number consistent numerical flux has been implemented based on the HLLC and the AUSM fluxes [46], [47]. Conservative variables at cell interfaces, required for the calculation of the fluxes, were determined using the MUSCL-Hancock reconstruction [48], second-order accurate in space. A fourth-order accurate, four-stage Runge-Kutta method has been selected for time integration, with a CFL criterion of 0.8 imposed for all the simulations performed.

LOx thermodynamic properties required by the density-based solver are derived from the Helmholtz energy EoS, which is calibrated within the temperature range 54.4 K≤T≤2000.0 K, for maximum pressure and density of p_{max}=82.0 MPa and ρ_{max}=1387.1 kg/m^3, respectively. The properties are organised into a thermodynamic table that may include a narrower range of values, depending on the application. The dimensionless form of the aforementioned EoS for the Helmholtz energy a, having as independent variables the density and the temperature [49] is:

$$\frac{a(\rho,T)}{RT} = a(\delta,\tau) = \alpha^0(\delta,\tau) + \alpha^r(\delta,\tau) \tag{3}$$

where $\delta=\rho/\rho_c$, $\tau=T_c/T$. From the expanded form of Eq. (3), where the dimensionless Helmholtz energy of the ideal gas a^0 and the residual Helmholtz energy a^r can be calculated using the correlations

reported by Kyriazis et al. in [38], all the necessary thermodynamic properties (pressure, internal energy, enthalpy and speed of sound) can be obtained, as function of density and temperature. Saturation conditions are identified by the Maxwell criterion, i.e. the pressure for which the Gibbs free energy of the liquid and vapour phases are equal for a given temperature. The fluid properties within the saturation dome are calculated by the mixture assumption, whereas the mixture speed of sound is determined from the Wallis speed-of-sound formula [41]. **Fig. 1** presents the variation of oxygen pressure (**Fig. 1a**), speed of sound (**Fig. 1b**) and internal energy (**Fig. 1c**) derived with density and temperature, as calculated employing the procedure in mention. The saturation curve in each plot is represented as a black dashed line.

Solving the Helmholtz EoS at each time step would incur considerable computational cost, as it requires root finding of non-linear equations. Hence, a tabulated-data technique, similar to that proposed in [50] has been implemented after explicitly solving the Navier-Stokes equations. A structured thermodynamic grid of 100,400 elements has been created, containing information for all the thermodynamic properties on each node defined by a density and internal energy value. The density range of the grid is $0.125 \leq \rho \leq 1263.8$ Kg/m^3 divided into 251 points of fixed $\Delta\rho$ = 5.055 kg/m^3, while the internal-energy range of the grid is $-171.14 \leq e \leq 165.51$ kJ/kg divided into 400 points of fixed Δe = 0.84161 kJ/kg.

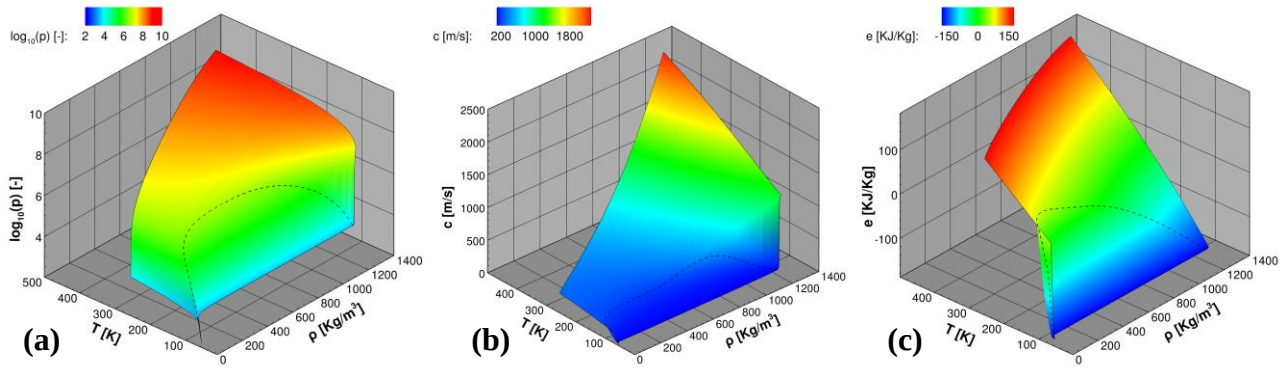

Fig. 1. *Three-dimensional phase diagrams for oxygen: (a) pressure, (b) speed of sound and (c) internal energy in terms of density and temperature.*

Once density and internal energy are calculated by the RANS equations, the corresponding element of the thermodynamic table is identified through numerical inversion from the above quantities. Any thermodynamic property φ of the table is then approximated by a finite element bilinear interpolation:

$$\varphi(\rho, e) = \sum_{n}^{nodes} N_n(\rho, e) b_n \tag{4}$$

where ϕ corresponds to pressure, temperature or speed of sound, required for the calculation of the fluxes in the density-based solver. Full details on the shape functions *N* employed and the calculations of unknowns *b* on each node *n* are reported in [38].

2.3 Turbulence closure

The Reynolds number characterising the flow has been found to be well within the turbulent regime for all the cases examined and ranging from 0.6 to 2.2m. The nozzle diameter was used as the characteristic length scale for the estimation of the Reynolds number, while an approximation of the velocity was made based on experimental values of the mass flow rate and the properties of the liquid phase at the saturation pressure corresponding to the injection temperature. The k-ω Shear Stress Transport (SST) turbulence model was therefore employed to account for contributions on fluid (or mixture) viscosity μ and thermal conductivity *k* due to turbulence effects. The specific

turbulence model has been demostrated to perform well in both moderately and highly-turbulent wall-bounded flows, where secondary-flow is also possible to arise [51].

With reference to the DES approach, the delayed detached eddy simulation model (DDES) was incorporated [52], which is formulated to switch between a RANS (k-ω SST) and a Large Eddy simulation (LES) Model, depending on the grid resolution and the local turbulennce length scale. Hence, the computational cost can be reduced in regions where the influence of turbulence in the flow field is expected to be minor. On the contrary, the model switches to a Smagorinsky-like subgrid model capable of resolving turbulent structures in high grid-density regions. It is important to highlight that the DDES formulation prevents grid-induced separation from occuring at regions of grid refinement inside attached boundary layers [53].

2.4 Domain discretisation and grid independence

A typical converging-diverging nozzle was selected as the computational domain, since experimental data with reference to cryogenic liquids are available in the literature for the specific layout. Since the orifice is axisymmetric, the domain was reduced to a wedge produced by rotating the nozzle layout, depicted in **Fig. 2**, around the symmetry axis by 5^o. A full 3-D domain representing the entire orifice volume (rotation of 360^o) was selected for DES, as the use of truncated domains and the imposition of a symmetry boundary condition was found to induce Coanda-like pseudo-instabilities [54] leading to an asymmetrical flow field at the diverging nozzle part. As also depicted in **Fig. 2**, the inflow section has been expanded upstream in both domains to impose the stagnation conditions of the experiment.

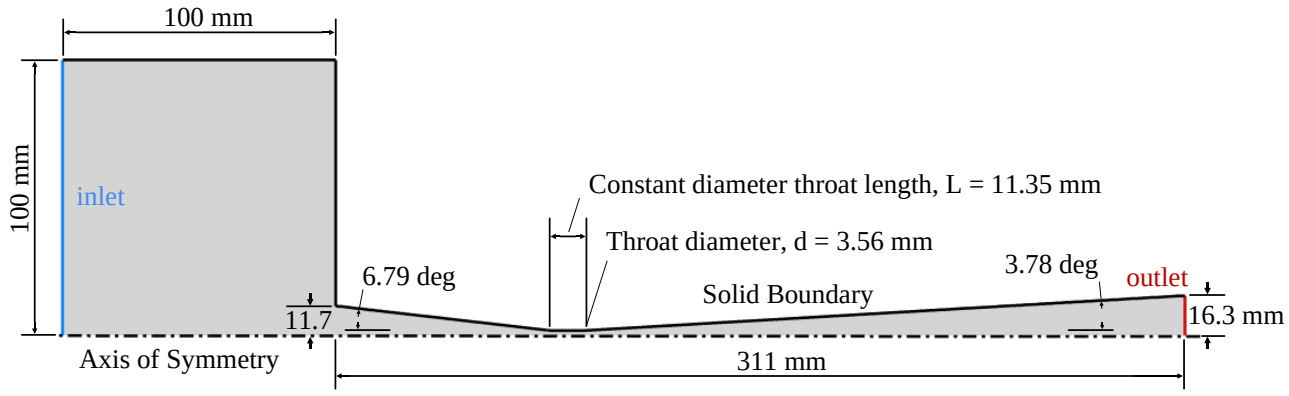

Fig. 2. *Geometry of the conical converging-diverging nozzle [10]. The inflow has been expanded upstream in order to impose the stagnation conditions of the experiment.*

A test case where severe jet expansion is expected to occur (refer to case 2 of **Table 3**) has been selected to evaluate the effect of grid density on the produced numerical results regarding the RANS simulations with the pressure-based solver being selected to conduct the grid independence study. **Fig. 3** presents the pressure (**Fig. 3a**) and volume vapour fraction (**Fig. 3b**) distributions, at the orifice symmetry axis, as produced by three numerical grids consisting approximately of 37, 60 and $100 \cdot 10^3$ cells, respectively. It is evident all three grids can capture the overall flow behaviour. It has been verified that the average discrepancy in the pressure values downstream the throat region between the intermediate and fine grids is of the order of 1.92 %, while the deviations in the vapour fraction values are approximately 0.12 %.

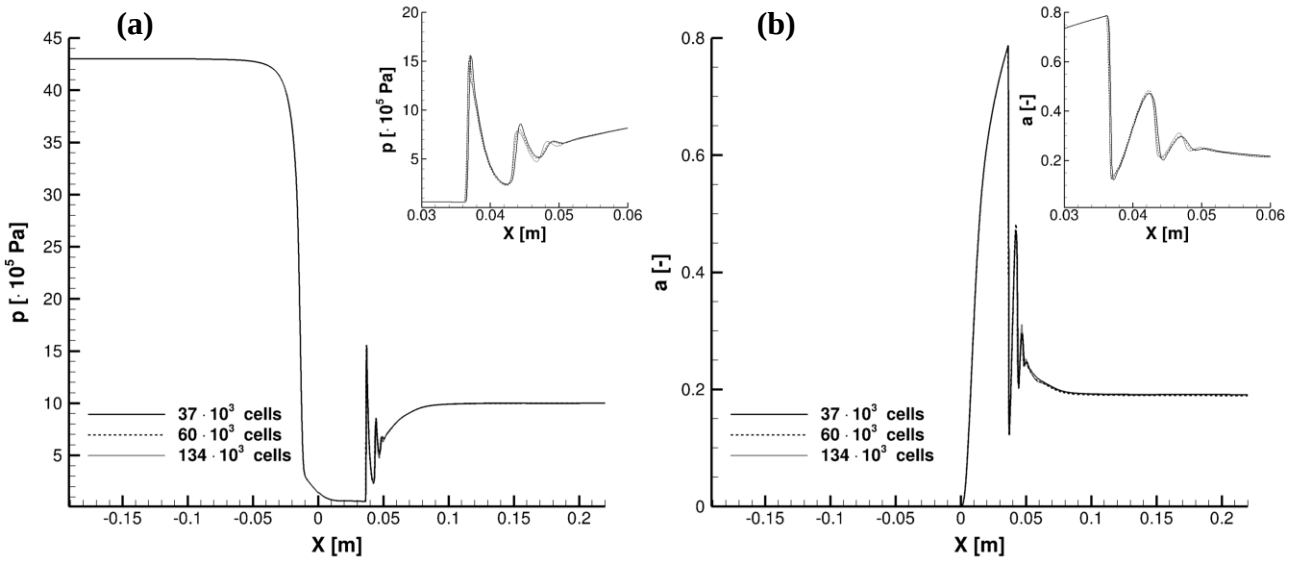

Fig. 3. *Grid independence study for RANS simulations: (a) pressure and (b) vapour volume fraction distributions at the orifice symmetry axis for grids of increasing cell count.*

Hence, the intermediate grid, the topology of which is depicted in **Fig. 4a** has been considered sufficient and it has been utilised by both solvers. As also shown in the detailed view of **Fig. 4a**, grid refinement layers were placed in the vicinity of the orifice wall resulting in a maximum y^+ distance of the order of 1.0 in the throat region. A much finer grid compared to the RANS simulations has been utilised for DES. The grid density was designated by the Taylor length scale:

$$\lambda_g = \sqrt{10} Re^{-0.5} L \tag{5}$$

where L is a characteristic length scale, selected as the nozzle throat diameter (d_t=3.55 mm) in the specific case. Inertial turbulent structures larger than the Taylor length scale are resolved through LES, while smaller viscous isotropic scales are modelled. The Taylor length scale for the cases examined lies in the range 50-120 μm. As depicted in **Fig. 4b**, a structured mesh with gradual refinement at the throat region has been generated for the DES investigation.

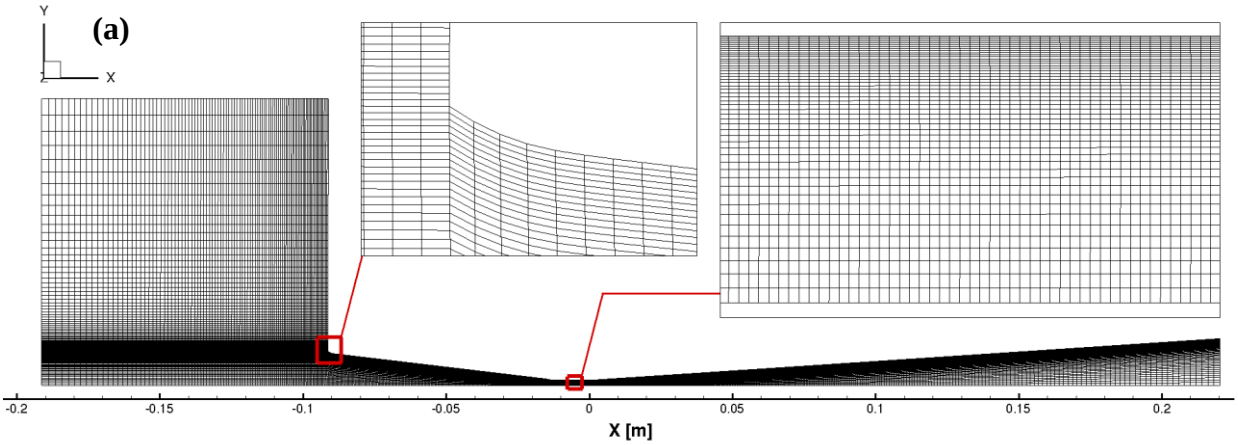

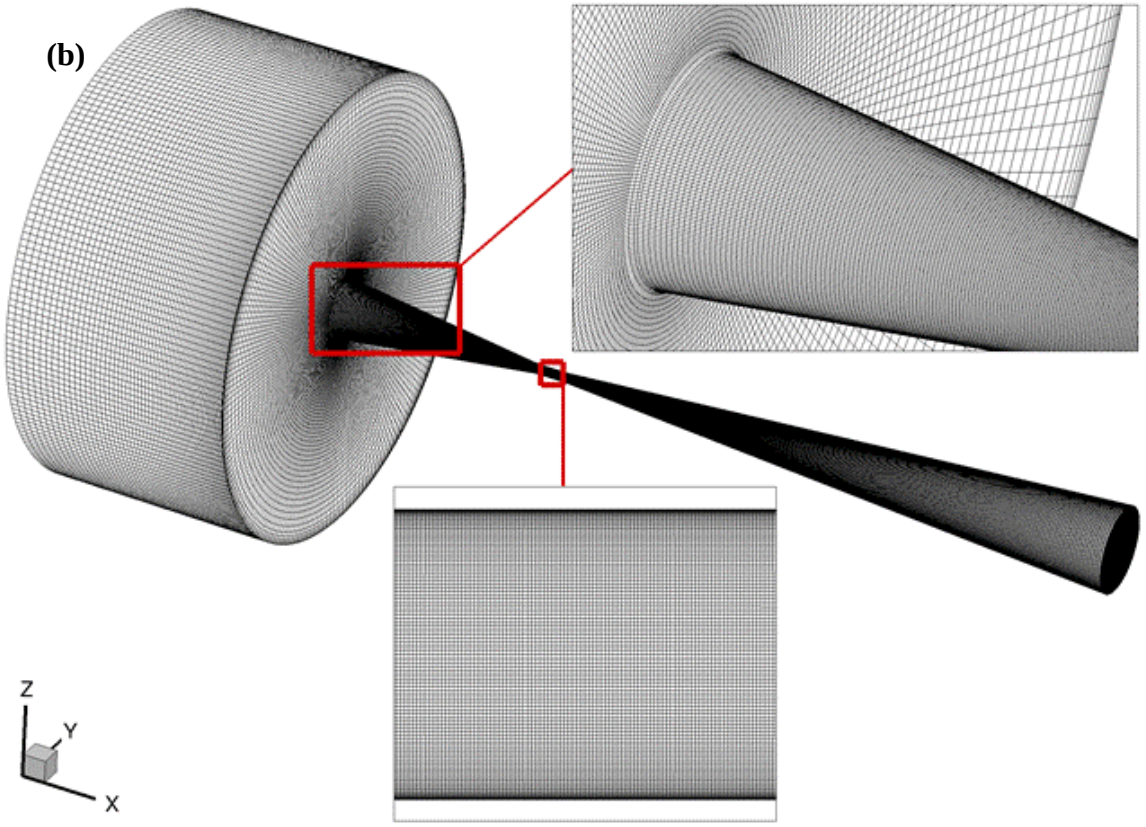

Fig. 4. *Computational grid employed for (a) RANS simulations and (b) DES. Detailed view of the nozzle inlet as well as the nozzle throat region are presented as insets for both grids.*

More specifically, the base resolution level at the upstream and downstream nozzle parts was progressively refined to the lowest value of the Taylor length scale at the throat region. Near-wall refinement was also applied leading to y^+ values of the order of 0.15 in the throat region. The overall cell count of the grid developed for the discretisation of the full 360° domain was approximately equal to $9.48 \cdot 10^6$ cells.

2.5 Boundary and initial conditions

Suitable boundary conditions complemented the governing equations, in order to replicate the physical conditions prevailing during the actual LOx-injection process. Dirichlet type boundary conditions, i.e. constant static pressure values corresponding to the actual operating conditions were imposed at the domain inlet and outlet for all the cases examined. Furthermore, a zero-gradient was imposed for the boundary-normal velocity component at the inlet, while the rest of the velocity components were set to zero. A no-slip condition was imposed at the nozzle wall. Referring to the energy-conservation equation, constant temperature or internal-energy values were imposed at the domain inlet and outlet for the pressure- and density-based solvers, respectively, owing to the different equation formulations implemented in each solver. The orifice wall was treated as adiabatic. At the outlet boundary, zero-gradient boundary conditions were set to all velocity components and transported quantities. The types of boundary conditions set for the examined cases are summarised in **Table 1**. The specific boundary-condition values of each variable and for each of the examined cases are presented in **Table** of section 3.

The RANS simulations were initialised assuming pure liquid (vapour faction $a=0$) in the entire domain, while the domain initial pressure and temperature were set equal to the respective inlet values. Quiescent fluid $\vec{u} = 0$) was assumed at the initial time instance. DES cases were initialised using the flow and temperature fields obtained from preliminary runs for the same conditions considering laminar flow of the liquid phase only, so as to provide the perturbations necessary for turbulence structures to develop. The initial conditions set are also summarised in **Table 1**.

Table 1. *Summary of boundary and initial conditions imposed for the numerical simulations.*

	Inlet		Outlet		Wall	
Pressure-based	$p = p_{in}$	$T = T_{in}$	$p = p_{out}$	$T = T_{out}$	$\vec{u} = 0$	$\partial T/\partial n = 0$
Density-based	$p = p_{in}$	$e = e_{in}$	$p = p_{out}$	$e = e_{out}$	$\vec{u} = 0$	$\partial T/\partial n = 0$

	Initialisation		
RANS	$\vec{u} = 0$	$T = T_{in}$	$a = 0$
DES	Solutions initialised with single-phase laminar flow		

3. Numerical simulations and results

The test cases examined in this study are summarised in **Table .** As can be seen, both sub- and supercritical injection pressures have been considered. More specifically, the pressure and temperature conditions of case 1 were obtained from the experimental campaign of Hendricks et al. [10] for which data regarding the pressure distribution along the orifice are available. The set of boundary conditions of case 2 was chosen as representative of a second-stage engine. Rocket-engine tests with the same outlet/chamber pressure have also been conducted on the Mascotte test bench of ONERA [13]. Finally, the conditions of case 3 were selected to be within the range of operation of the LOx turbo pump of the Vulcain-2 engine of Arianne 5 heavy-lift space launch vehicle [55], [56] and higher than the combustion chamber pressure [3], while maintaining the same pressure difference as in case 1. The rationale was to pinpoint the significant variation in expansion dynamics between sub- and supercritical pressure injection despite the similarity in macroscopic flow parameters. Simulations for all cases were performed with the use transient solvers, yet it was confirmed that the respective flow and temperature fields reached to steady-state solutions in most cases.

Table 2. *Matrix of test cases examined. It must be noted that temperature lies in the subcritical regime for all cases.*

Case	$p_{in}\cdot10^5$ [Pa]	$p_{out}\cdot10^5$ [Pa]	T_{in} [K]	$e_{in}\cdot10^3$ [m^2kg/s^2]	Pressure Regime	Phase-change model
1	11.4	2.6	115.3	-361.01	Subcritical	Helmholtz EoS / Hertz-Knudsen Eq. (2)
2	43.0	10.0	93.6	-400.44	Subcritical	Helmholtz EoS / Hertz-Knudsen Eq. (2)
3	133.0	124.2	93.6	-403.29	Supercritical	Helmholtz EoS / NIST

3.1 Code validation

The pressure-based solver employing the Hertz-Knudsen phase-change model has been extensively validated with reference to internally and externally flashing flows considering water as the working medium in a previous work of the authors' group [37]. More specifically, the model has been demonstrated to accurately capture phase-change in a converging-diverging nozzle similar to the one of the present study, a (throttle) nozzle with an abrupt contraction and a rapidly depressurising duct (pipe blow-down). To further demonstrate the accuracy of the Hertz-Knudsen model, additional simulations have been performed for the geometry described in

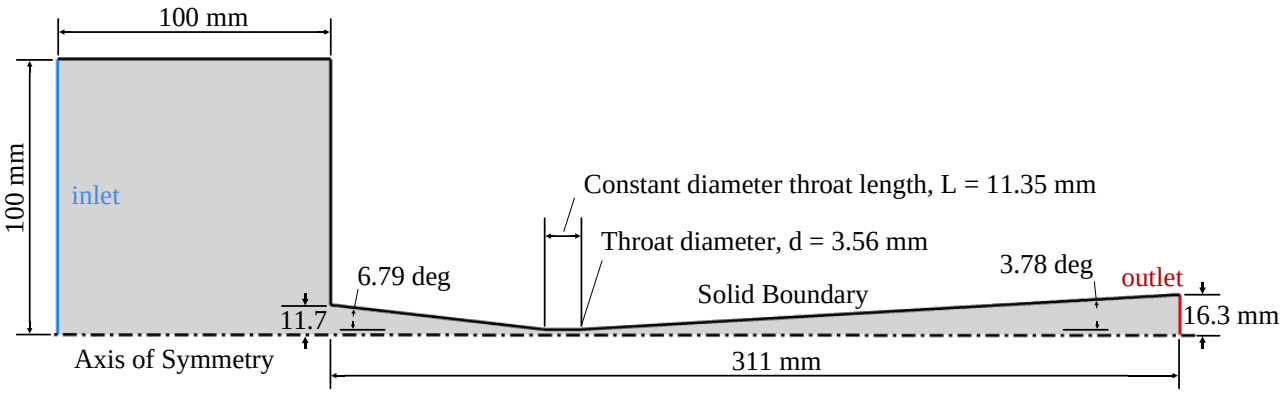

Fig. 2 and the numerical predictions for LOx mass flow rate are compared in **Table 3** against experimental data available from [10]. As can be seen, good agreement between the numerical and experimental data is achieved for a wide range of conditions in the subcritical regime.

***Table 3**. Comparison between experimental and numerical results. The Hertz-Knudsen model was utilised for the flow simulations.*

Boundary conditions			**Experimental**	**Numerical**	**Deviation**
$p_{in}\cdot10^5$ **[Pa]**	$p_{out}\cdot10^5$ **[Pa]**	T_{in} **[K]**	$\dot{m}_{exp}$ **[kg/s]**	$\dot{m}$ **[kg/s]**	**from** $\dot{m}_{exp}$
49.2	7.1	134.0	0.669	0.677	1.25%
38.9	6.1	134.2	0.542	0.541	-0.17%
25.1	3.6	116.1	0.541	0.560	3.58%

Furthermore, the density-based algorithm has been validated in previous works with reference to bubble- [38], and droplet-dynamics [57] simulations, while the accuracy of the tabulated technique based on Helmholtz energy EoS has been verified with reference to the properties of n-dodecane [38]. An additional validation study has been set up in order to further evaluate the capability of the density-based solver with the Helmholtz EoS thermodynamic closure to capture wall-bounded LOx flows. A computational domain corresponding to a reference converging diverging nozzle of circular cross section was realised and the numerical results were compared against an 1-D HLLC solver for the Euler equations considering an EoS of the form $p = f(\rho, e)$, which can be provided in either analytically [48] or in a tabular form [38]. The orifice cross-sectional area S varies with its length L according to the relation $S(L) = 0.01 \cdot L^2 + 0.01$ for $L \in [-2,2]\ m$. A 5º wedge of the geometry was considered as the computational domain, discretised by a structured grid of 5200 cells. The cell size was uniform and equal to 10.0 mm along the longitudinal direction, while it varied between approximately 0.9 mm (throat region) and 4.3 mm (upstream and downstream parts) along the radial direction. The density and temperature at the domain inlet were set equal to $\rho_{in} = 817.07\ Kg/m^3$ and $T = 143\ K$, respectively, which will lead to an inlet pressure of $53.87\cdot10^5$ Pa, while the outlet pressure was set to $16.35\cdot10^5$ Pa. As made evident by **Fig. 5**, the obtained numerical solution and the reference 1-D solution are in excellent agreement regarding all the plotted quantities. Due to subsonic flow conditions in the entrance, the flow accelerates in the converging part (**Fig. 5a**). The expansion of the of the two-phase jet leads to further acceleration and transition to supersonic velocities (**Fig. 5b**), while the supersonic region is extended all the way down until the exit of the orifice without the manifestation of a shockwave system, as made clear by the pressure distribution of **Fig. 5c**. Almost full liquid vaporisation has occurred by the outlet location, as depicted in **Fig. 5d**. It has to be noted that, apart from this initial validation study, further comparisons of the numerical results have been conducted against available experimental data, as discussed in the following section.

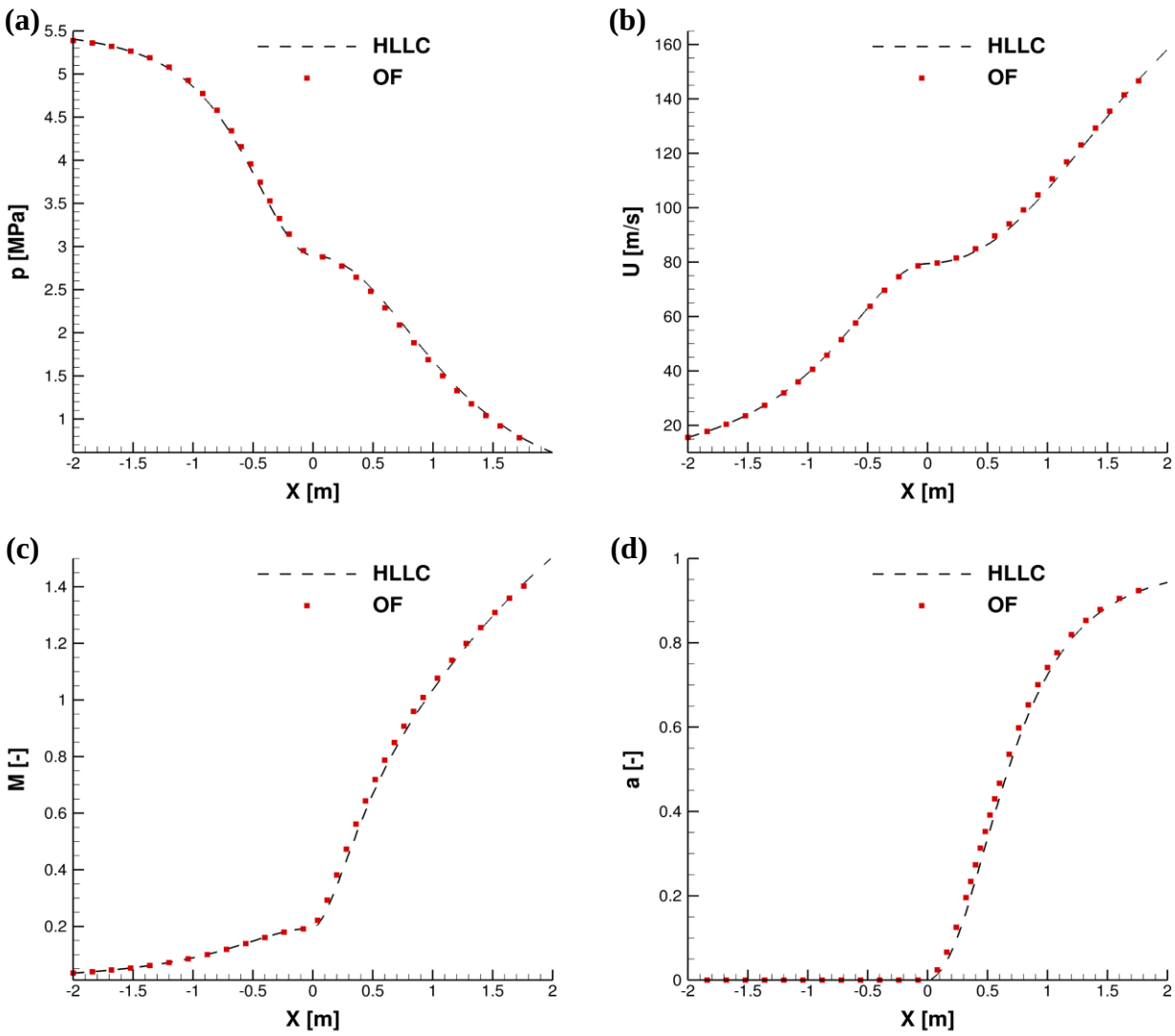

Fig. 5. *Validation of the density-based solver (OF) for the converging-diverging nozzle case: Numerical results for (a) pressure, (b) velocity magnitude, (c) Mach number (d) vapour volume-fraction distributions along the orifice symmetry line and comparison against the predictions of the 1-D solver (HLLC).*

Finally, the accuracy of the employed pressured-based solver using the REFPROP database to replicate phase change in the supercritical regime has been verified against the quantitative measurements of Mayer et al. [58] for a N_2 jet, since quantitative data on supercritical LOx could not be obtained from the open literature. The jet enters at a velocity of 5.4 m/s a chamber where supercritical pressure (3.98 MPa) and temperature (137 K) conditions persist. The Reynolds number characterising the injection is equal to $1.53 \cdot 10^5$. **Fig. 6** depicts the average density distribution along the jet axis obtained through 3D LES, while the averaged density field is presented in the figure inset. It is demonstrated that very good agreement is achieved between numerical and experimental results.

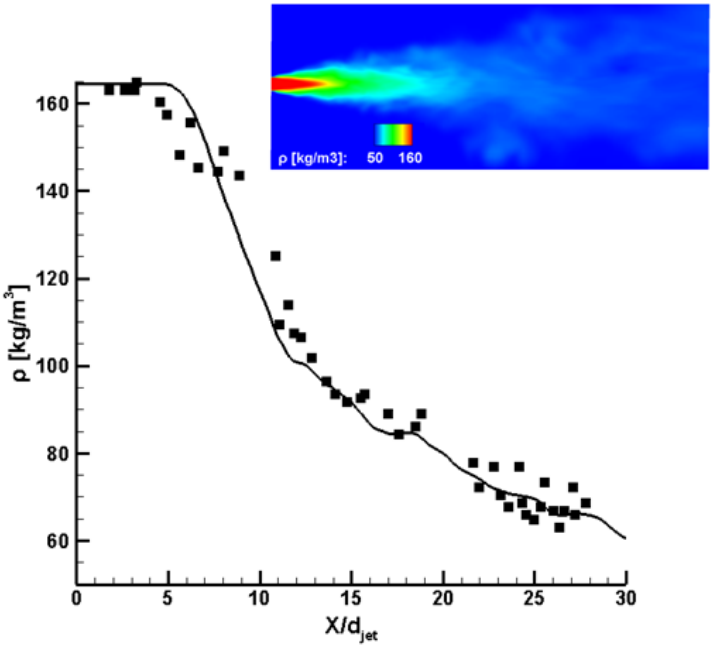

Fig. 6. *Validation of the pressure-based solver using NIST-REFPROP database: Comparison of numerical predictions of the average N_2-jet density distribution at the jet axis (solid line) against experimental data (symbols) [58]. The average density contour plot is depicted in the inset.*

3.2 Simulations in the subcritical regime

The numerical results corresponding to cases 1 and 2 of **Table** are discussed in this section. **Fig. 7** illustrates the distinct flow features as predicted by the two solvers for case 1. The rapid fluid pressure drop in the throat region and downstream is clearly shown in the contour plots of **Fig. 7a**. It must be noted that the top and bottom frames correspond to the predictions of the pressure- and density-based solvers, respectively. A pressure minimum is reached at the orifice diverging part followed by the manifestation of a shock wave. The pressure re-develops to its outlet value further downstream. As shown in **Fig. 7b**, the flow accelerates in the converging part, nevertheless the flow velocity is adjusted by the local speed-of-sound velocity, which is in turn designated by the composition of the two-phase mixture. The flow further acceleration downstream the nozzle throat corresponds to the expansion of the in-nozzle choked flow (M=1). Almost full liquid vaporisation occurs at the diverging part of the geometry (**Fig. 7c**), thus, the value of the mixture Mach number also increases (also highlighted in section 3.4). Furthermore, fluid temperature decreases in the region, as shown in **Fig. 7d**, due to the transformation of sensible to latent heat required for bubble nucleation. Although, the physical-quantity fields predicted by the two solvers are qualitatively similar, distinct discrepancies can be detected, especially in the vapour fraction (**Fig. 7c**) and temperature fields (**Fig. 7d**). Those discrepancies are rooted in the inherent difference in the way that the rate of phase-change is imposed in the two solvers. In essence, through the adoption of an EoS, an infinite phase-change rate is imposed by the density-based solver. On the contrary the rate in the pressure-based counterpart is inherently finite due to the adoption of a phase-change model. Hence, the density-based solver predicts more rapid vapour formation in the nozzle throat (**Fig. 7c**), with noticeable after-effects in the flow and temperature fields.

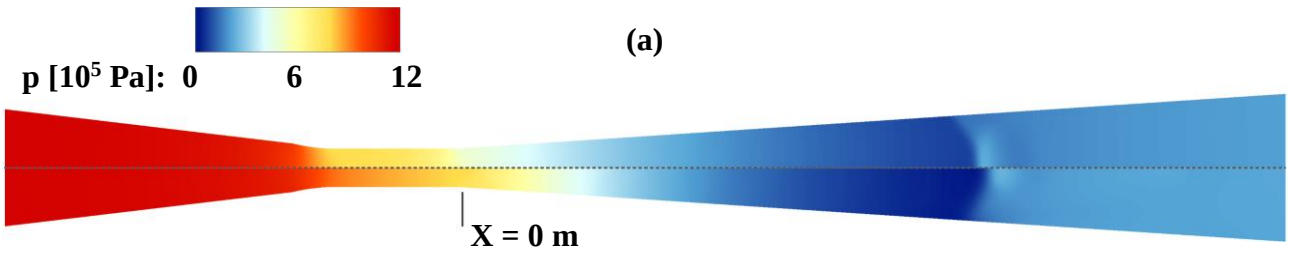

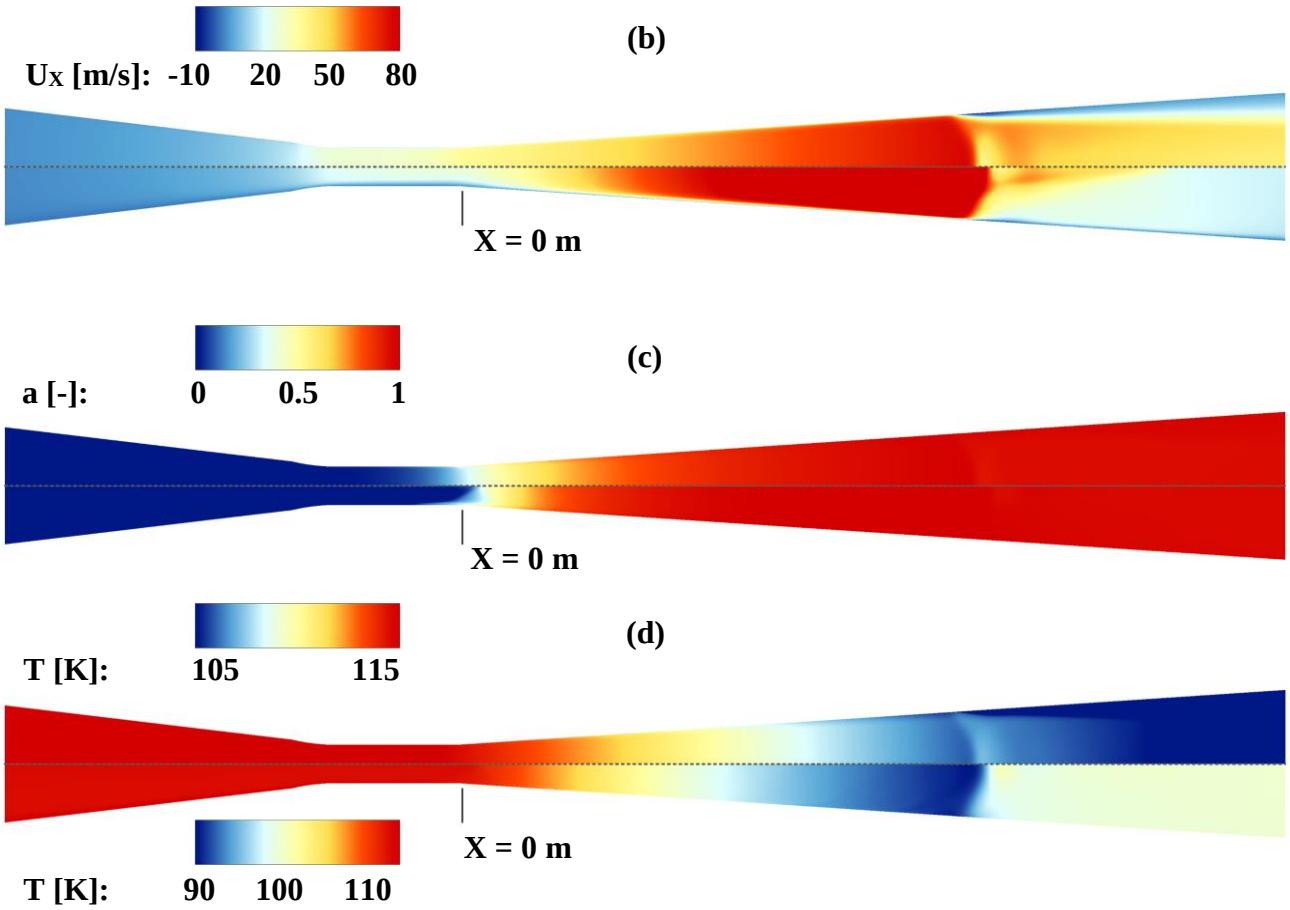

Fig 7. *Contour plots of the (a) pressure, (b) velocity (c) gaseous volume fraction and (d) temperature field in the nozzle-throat region for case 1 of* ***Table*** *3. It is noted that different variable ranges have been used in frame (d) to enhance clarity. Upper frames depict predictions produced using the Hertz-Knudsen (λ=0.7) phase-change model (Eq. 2), while lower frames those produced using the Helmholtz EoS (Eq. 3). All contours represent the part of the nozzle from* $X = -0.045\ m$ *to* $X = 0.08\ m$.

Fig. 8 depicts the distribution of physical quantities at the orifice axis of symmetry, as predicted by the two solvers for case 1, as well as the experimental data available by Hendricks et al. [10]. As it can be seen in **Fig. 8a**, the numerical results from both solvers are in good agreement with the experimental values regarding the axial pressure distribution. The profiles show an abrupt pressure drop initiating at the throat area along with a flow acceleration (**Fig. 8b**). The magnitude in the imposed phase-change rate leads to noticeable variation between the axial velocity distributions obtained by the two numerical approaches. It is reminded that the thermodynamic closure of the density-based solver is based on tabulated data, intrinsically imposing thermodynamic equilibrium between the phases. On the contrary, phase-change in the pressure-based solver is designated by the source term in the vapour advection equation. It was verified though preliminary simulations that adopting an accommodation coefficient λ value (refer to **Eq. (2)**) of 0.7 gives the closest agreement between the predictions of the pressure-based solver and experimental data of Hendricks et al. [10], which suggests a moderate yet clear departure from thermodynamic equilibrium. As already mentioned, the increased phase-change rate is the cause for the higher flow axial velocity (**Fig. 8b**) and vapour-fraction distributions in the throat region (**Fig. 8c**) obtained by the density-based solver. A higher vapour extent in the two-phase mixture forming in the nozzle throat, affects the local speed-of-sound values and consequently the mixture acceleration in the diverging part. Likewise, temperature drop is also linked to phase change; thus, the higher vapour formation observed in the

density-based solver is associated with more extensive transformation of sensible to latent heat and consequent temperature decrease, as shown in **Fig. 8d**.

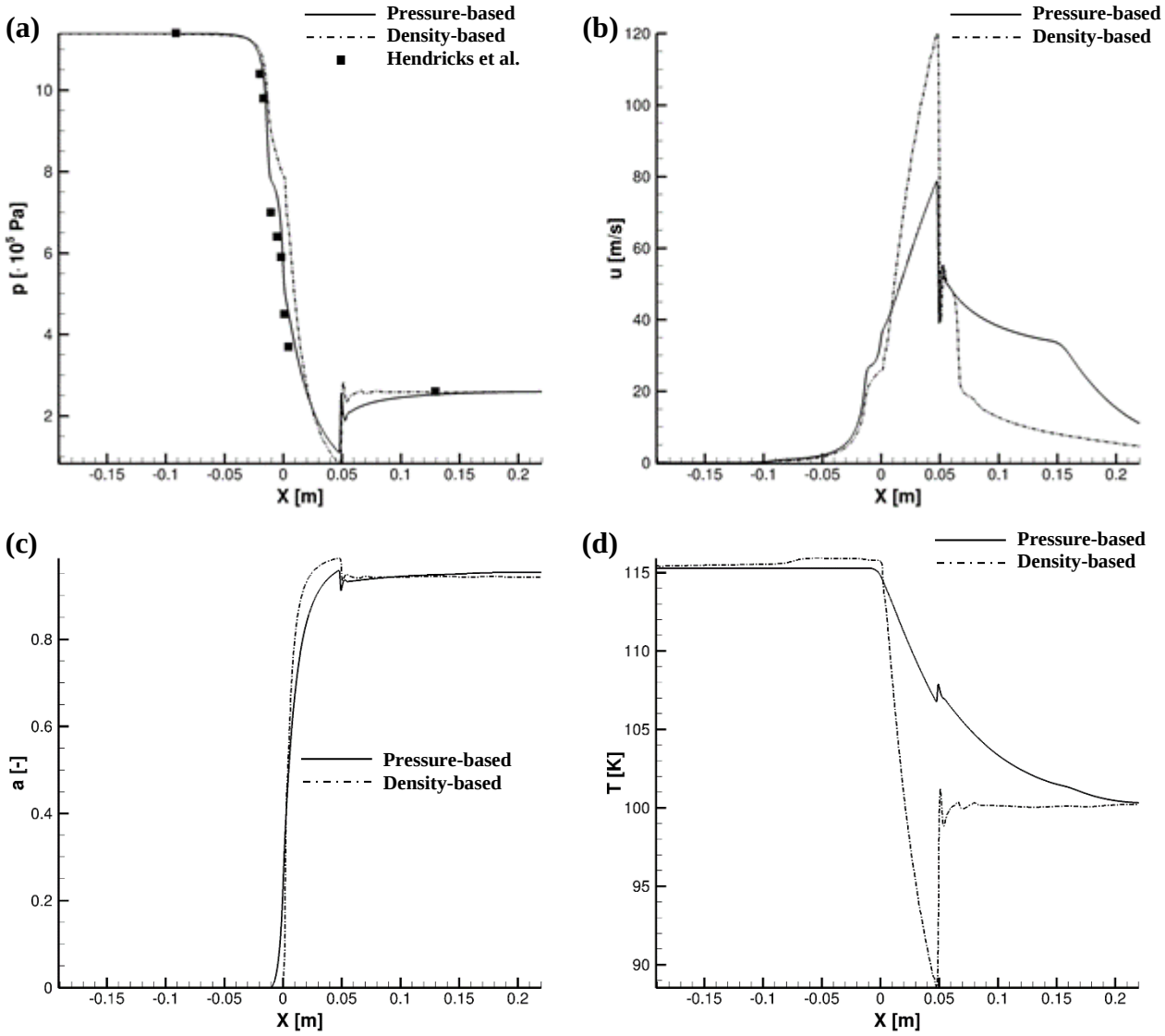

Fig. 8. *(a) Pressure, (b) velocity, (c) vapour-volume fraction and (d) temperature distributions at the orifice symmetry axis, as predicted by the two numerical approaches for case 1 of* ***Table 3****.*

As an additional study of evaluating the accuracy of the proposed numerical approaches to replicate phase-change, the predicted mass flow rate through the nozzle has been compared against the measured value $\dot{m}_{exp}$ (=0.27 kg/s) by Hendricks et al. [10], for case 1 of **Table 3**. The discrepancies between numerical and experimental data are summarised in **Table** . As can be seen, the formulation based on the phase-change model achieves a closer agreement compared to the employing tabulated thermodynamics. In agreement with established knowledge regarding the departure of flashing flows from thermodynamic equilibrium ([59]–[61]) the density-based solved imposing an infinite rate under-predicts the mass-flow rate, yet since only a moderate departure from equilibrium is experienced in the specific geometrical layout, as also shown in [37], the relevant results are still of acceptable accuracy.

Table 4. *Evaluation of LO_X mass-flow rate value through the orifice predicted by the two solvers for case 1 of* ***Table*** *.*

Phase-change mechanism	**Predicted $\dot{m}$ [kg/s]**	**Deviation from $\dot{m}_{exp}$**

Pressure-based, Eq. (2)	0.263	-2.59 %
Density-based, tabulated thermodynamics	0.247	-8.36 %

The numerical results for case 2 of **Table** , characterised by a smaller pressure difference along the nozzle boundaries compared to case 1, are presented in **Fig. 9**. A rapid fluid pressure drop at the nozzle-throat region followed by the manifestation of a series of pressure peaks at the diverging part is illustrated, particularly for the pressure-based solver (**Fig. 9a**, upper panel). The presence of this series of shock cells, which will be thoroughly discussed in section 3.4, is a clear characteristic of an under-expanded jet and confirms the resemblance in expansion dynamics between two-phase flashing and supersonic gas jets [62]. Comparison between the upper and lower panels of **Fig. 9a** reveals that the locations of the first Mach disk (annotated as region 1) and oblique shock-waves (region 2) are clearly discernible in the pressure field produced by the pressure-based solver (upper panel). On the contrary, the respective features cannot be clearly defined in the plot corresponding to the density-based solver. It must be noted that the specific solver converged to a transient, oscillating flow field, where the shockwave locations differed slightly over successive time instances, unlike the pressure-based counterpart that predicts an invariable flow field. Hence, the difference in shockwave dynamics is reflected in the time-averaged results presented in **Fig. 9**. **Fig. 9b** depicting the axial velocity field also demonstrates a more significant flow deceleration at the locations of the normal and oblique shockwaves predicted by the pressure-based solver.

In a similar manner, distinct features emanating from the local pressure field are evident in the contour plots of the vapour-volume fraction depicted in **Fig. 9c**. Phase-change is not as extensive as in case 1 of **Table ,** as it is disrupted due to the higher pressure to which the flow must equilibrate, in essence, through the formation of the complex shock-cell system. Once again, abrupt gradients of the vapour volume faction values in pressure-peak locations are evident in the predictions of the pressure-based solver, while the respective field produced by the density-based solver appears smoothened and somewhat ‘smeared’, owing to the averaging of the oscillating two-phase flow field. As expected, fluid temperature decreases in the throat region, as shown in **Fig. 9d**, due to phase-change. Nevertheless, subsequent temperature increase takes place further downstream, in the nozzle diverging section, due to the compressible nature of the fluid, as the flow re-adjusts to higher pressures. Overall temperature diferrences are considerably more moderate compared to case 1.

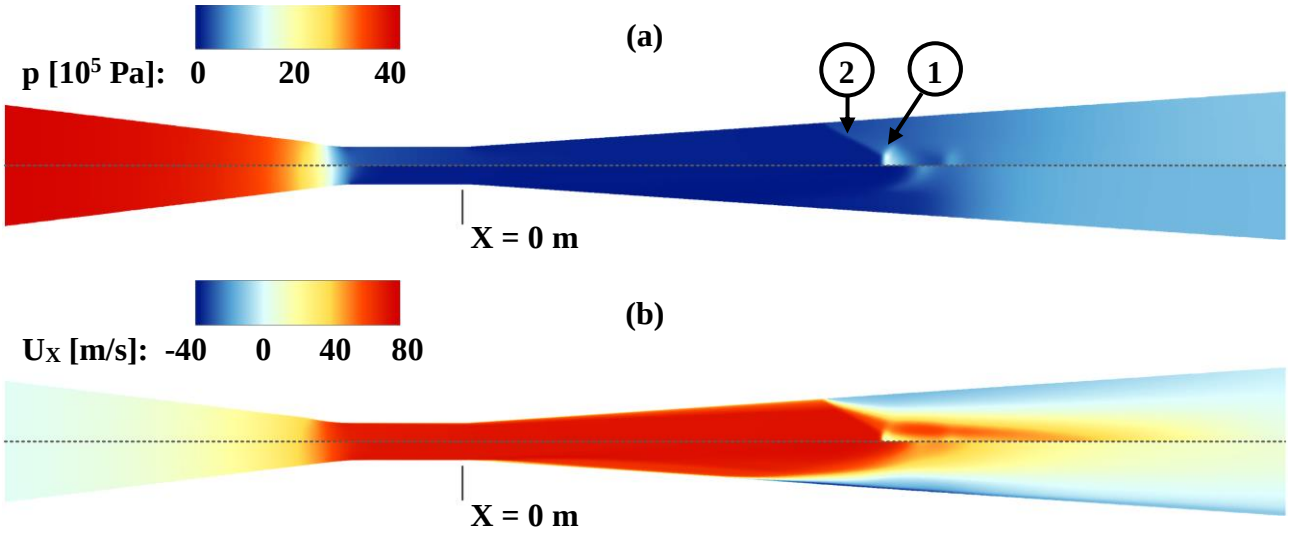

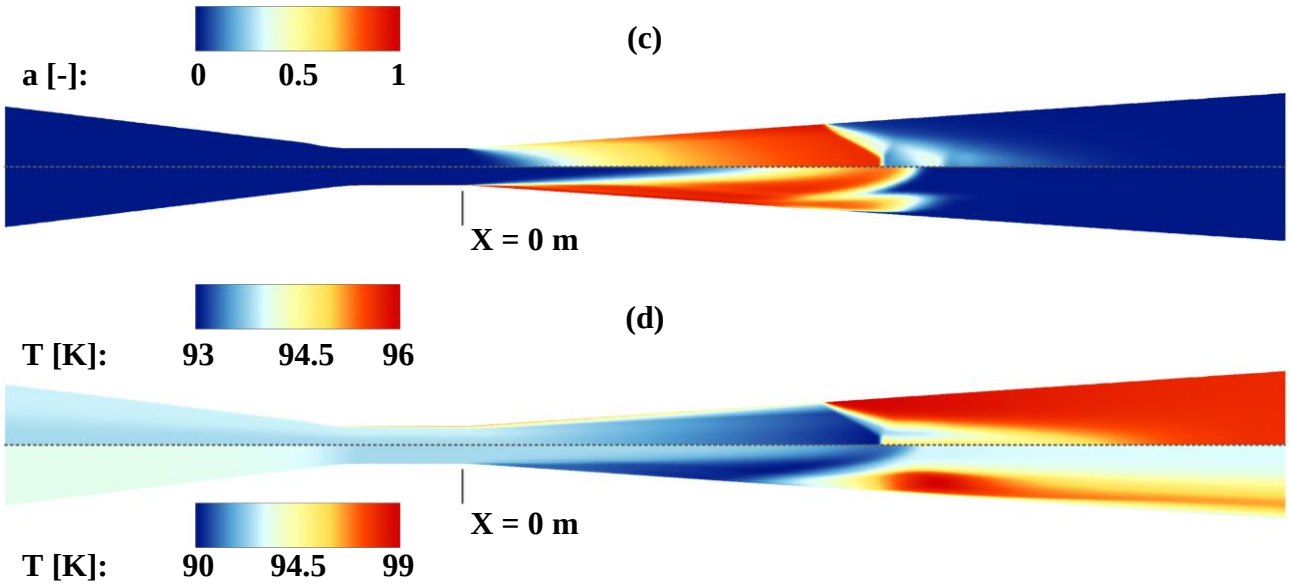

Fig 9. *Contour plots of the (a) pressure, (b) velocity (c) vapour-volume fraction and (d) temperature fields in the nozzle throat region for case 2 of* ***Table*** *. It is noted that different variable ranges have been used in frame (d) to enhance clarity. Upper and lower panels depict predictions produced using the pressure- and density-based solver, respectively. All contours represent the part of the nozzle from* $X = -0.045\ m$ *to* $X = 0.08\ m$.

Fig. 10 depicts the axial distributions of physical quantities of interest at the orifice symmetry axis, as predicted by the two solvers for case 2. The pressure profiles of **Fig.10a** highlight the discrepancies in the predictions of the two solvers, since the pressure peaks are much more clearly defined in the results produced by the pressure-based solver denoting the presence of two normal shockwaves. The transient nature of the results of the density-based solver will not allow for the shock formations to become evident on the presented time-averaged results as the shock axial location remains unsteady. The distinct features of the pressure field designate the respective velocity (**Fig. 10b**) and vapour-fraction distributions (**Fig. 10c**). Oscillations in both distributions can be detected at $X \approx 0.08$ m where regions of high and low pressure overlap, hence adjusting flow acceleration and phase change. The two solvers are in good agreement on the prediction of the maximum axial velocity immediately after the throat area. Unlike case 1 that corresponded to a lower outlet pressure outlet, full vapour condensation occurs in the diverging section and pure liquid exits the nozzle. The temperature distribution of **Fig. 10d** reveals that the mixture cools down only moderately during expansion, as phase-change is disrupted by the pressure re-adjustment to higher values. Once again, due to the infinite phase-change imposed the temperature drop experienced is higher for the density based-solver.

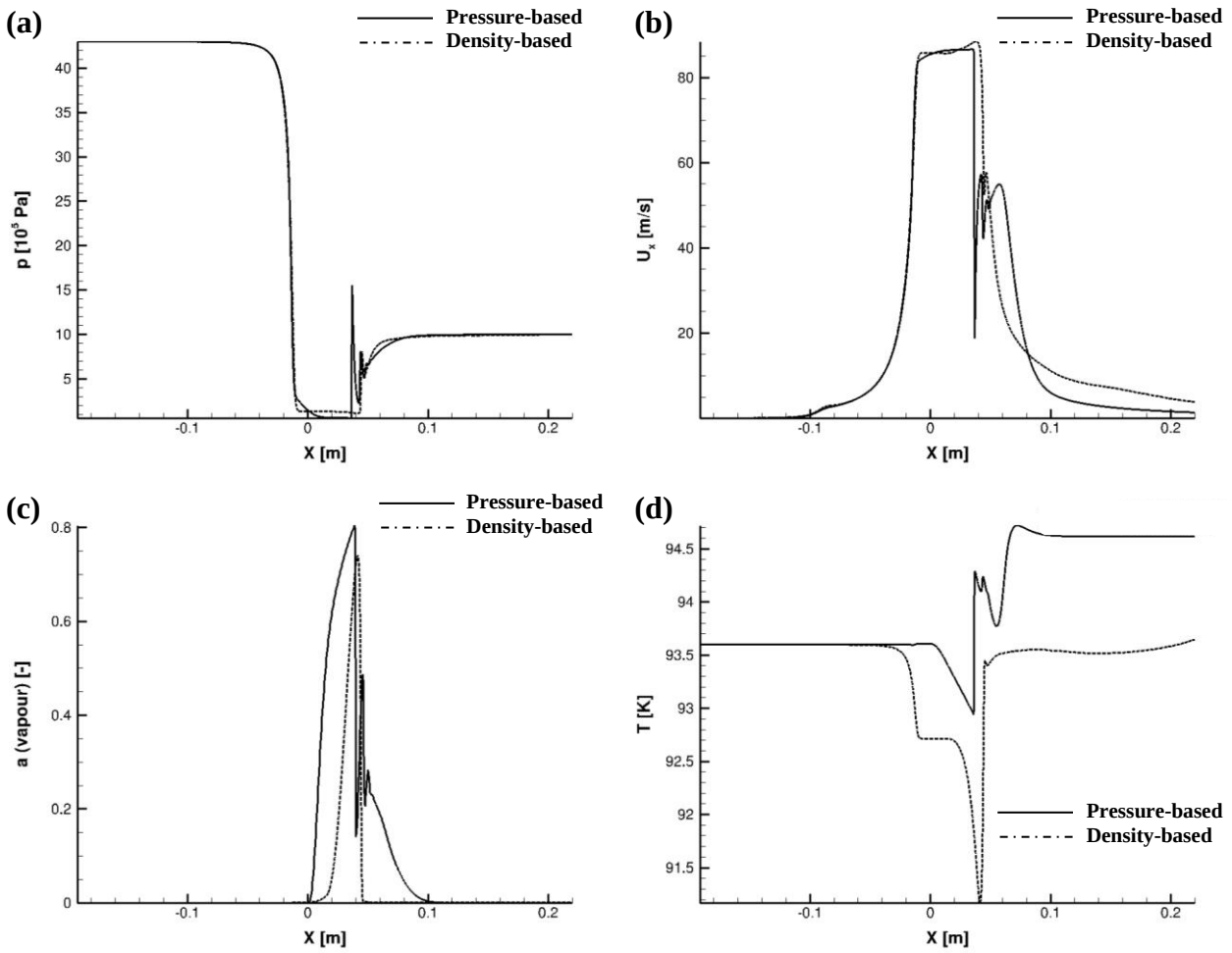

Fig. 10. *(a) Pressure, (b) velocity, (c) vapour volume fraction and (d) temperature distributions at the orifice symmetry axis, as predicted by the two thermodynamic approaches for case 2 of* ***Table*** *.*

3.3 Simulations in the supercritical regime

Fig. 11 illustrates the distinct features of the flow field with regards to supercritical pressure injection (case 3 of **Table**). Similar to the subcritical cases, the predictions of the two solvers are comparatively presented in each plot of **Fig. 11**. As can be observed, the two numerical approaches are in agreement regarding the overall flow evolution, which exhibits smooth transitions regarding all the plotted quantities. As expected, pressure decreases at the nozzle throat (**Fig. 11a**), as the flow accelerates due to the geometrical constriction (**Fig. 11b**). The fluid retains liquid-like densities throughout the domain (**Fig. 11c**), while the moderate depressurisation at the contracting section is accompanied by a mild temperature drop (**Fig. 11d**). All the distinct flow features identified for the two subcritical cases, i.e. flow expansion and formation of shockwaves, are completely absent in the supercritical regime.

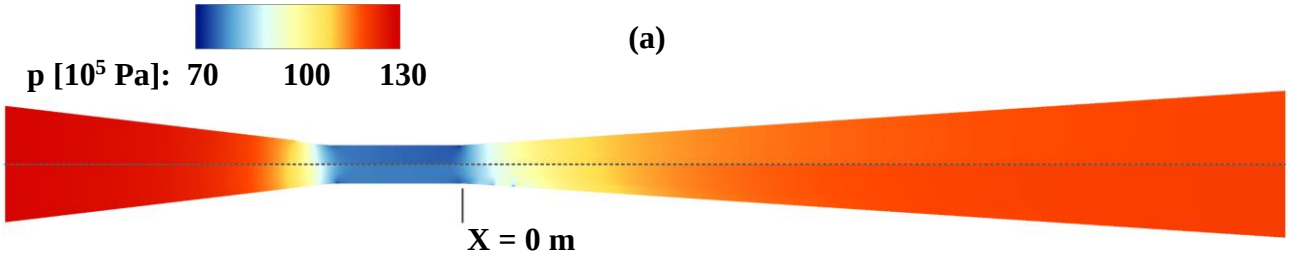

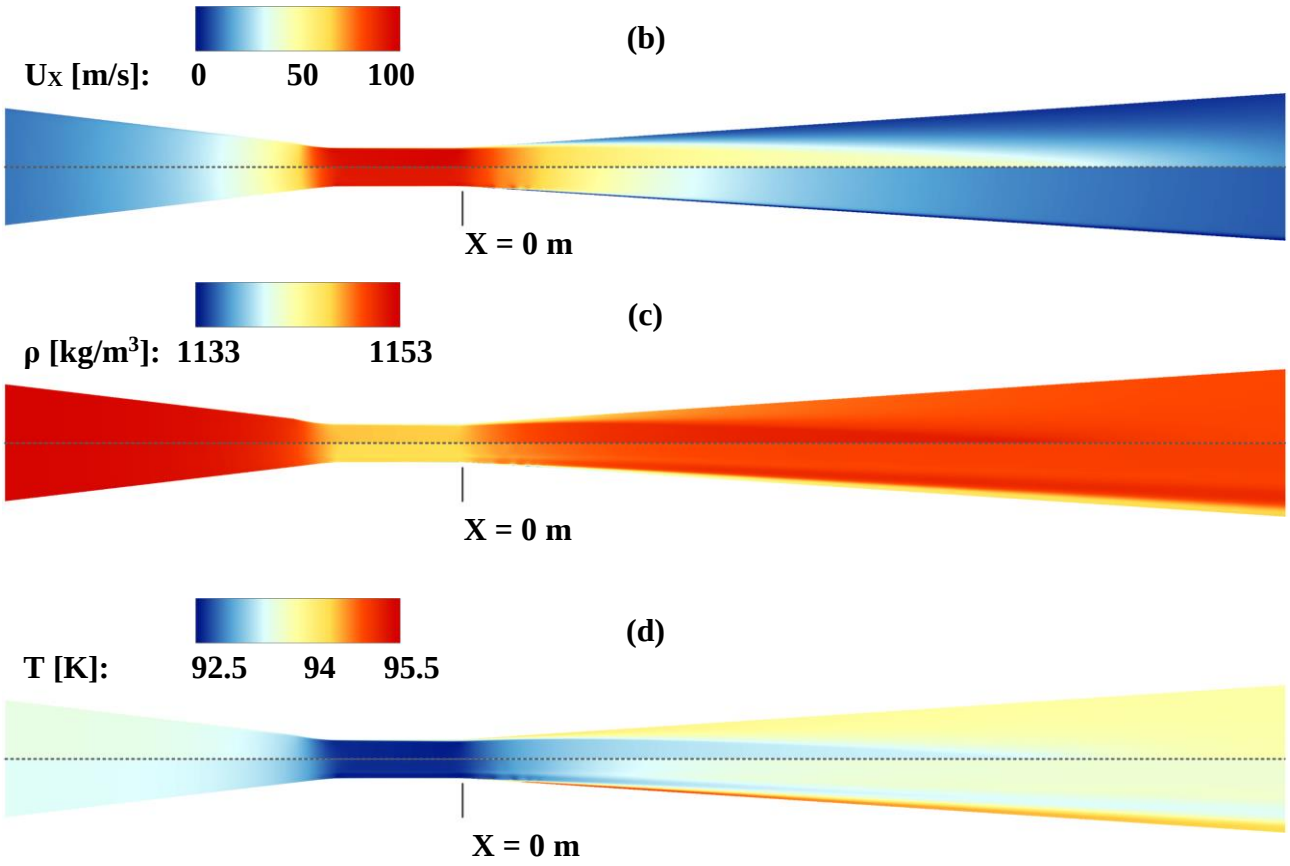

Figure 11. *Contour plots of the (a) pressure, (b) velocity, (c) density and (d) temperature field for supercritical injection (case 3 of* ***Table*** *). Upper frames of each figure depict the predictions produced using the pressure-based solver and the NIST database, while lower frames those produced using a density-based solver and tabulated data produced by solving the Helmholtz EoS. All contours represent the part of the nozzle from* $X = -0.045\ m$ *to* $X = 0.08\ m$.

Similar to the sub-critical cases discussed earlier, **Fig. 12** presents in a comparative manner the distributions of the quantities of interest along the symmetry axis of the nozzle. The distributions of pressure (**Fig.12a**) and density (**Fig.12c**) demonstrate that since the entire flow process takes place at supercritical pressures, the fluid possesses liquid-like density, hence, compressibility effects are absent. Since all quantities are correlated to the medium density, the distributions of axial velocity (**Fig.12b**) and temperature are also in good agreement (**Fig.12d**). The pressure-based solver predicts slightly lower density values in the throat region than the density-based one. In this specific case, where both solvers employ tabulated thermodynamics, the differences in the results can be attributed to minor differences in the levels of accuracy and refinement of the tables from which thermodynamic properties are obtained.

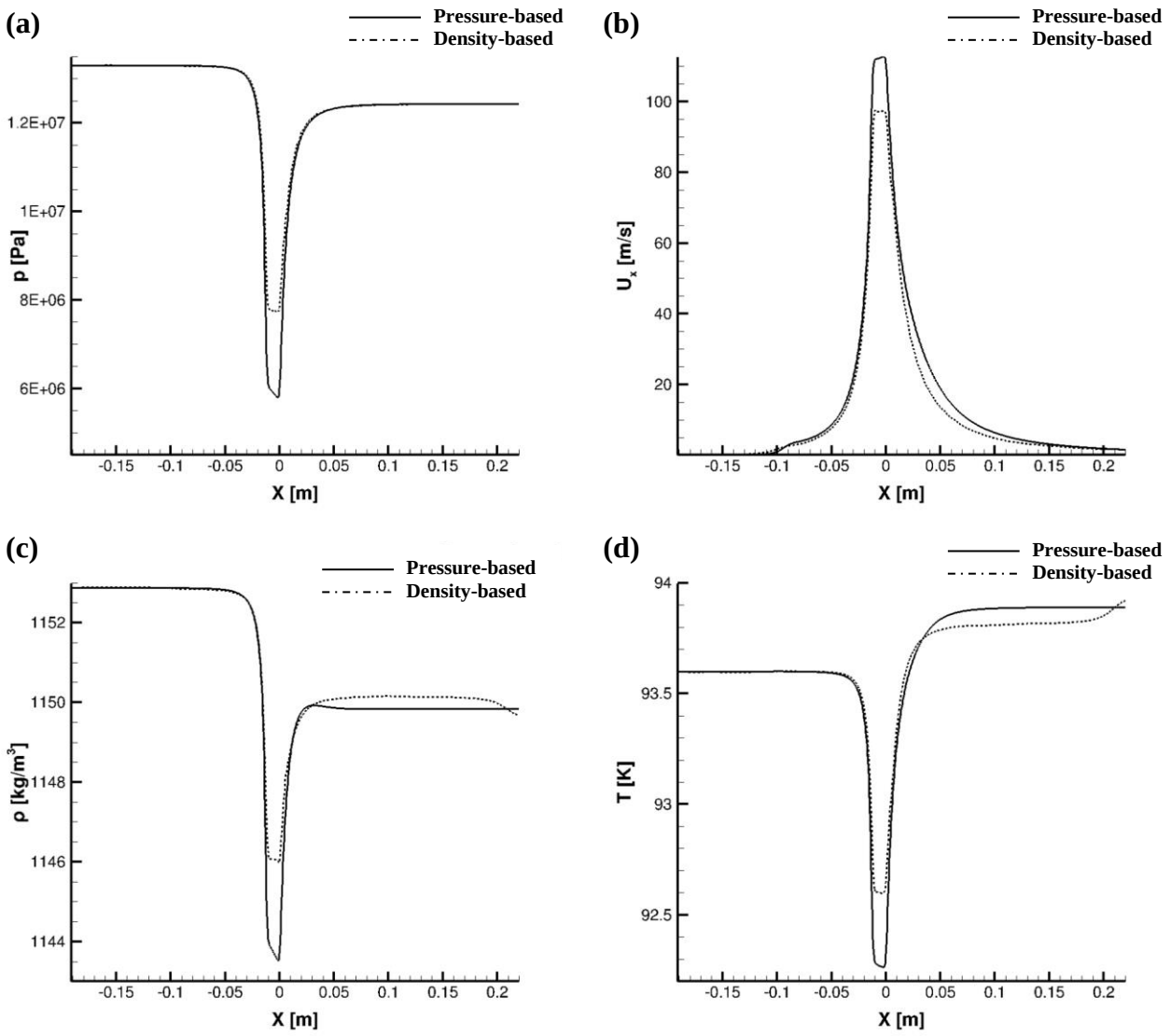

Figure 12. *Distribution of (a) pressure, (b) velocity, (c) density and (d) temperature at the orifice symmetry axis, as predicted by the two solvers adopting different thermodynamic approaches for case 3 of* ***Table*** *.*

3.4 Comparison of expansion dynamics for the two regimes

A comparison between **Figs. 13a-b** and **Fig. 13c** reveals that the flow evolution in the nozzle throat and downstream diverging region exhibits a highly variable behaviour between the subcritical and supercritical cases examined. In the subcritical pressure regime, the flow first becomes supersonic in the interior of the domain where sound speed is lowest. Shock waves occurring within the nozzle can interact with the boundary layer flow and result in a 'shock train' and a sequence of subsonic and supersonic flow, previously observed in single-phase nozzles ([63], [64]), refer especially to **Fig. 13b**. Flow through the Mach stem is brought to subsonic velocities, while flow through the annular oblique shocks remains supersonic. The pressure across the boundary between these two regions is matched, but temperature, entropy and velocity change almost discontinuously immediately downstream of the point where the oblique shock, Mach disk and reflected shock intersect, referred to as the triple point in relevant flow studies ([65], [66]). Turbulent mixing takes place across this boundary, eventually bringing the core of the flow back to supersonic velocities prior to the next shock cell. In the case of supercritical pressure (**Fig. 13c**), flow accelerates due to the geometry of the nozzle throat, without exceeding a Mach number of 0.2 at any point. In the diverging part the flow decelerates with no discontinuities in any of the variable fields. As mentioned also in paragraph 4.2, the flow field exhibits no appreciable distinct features.

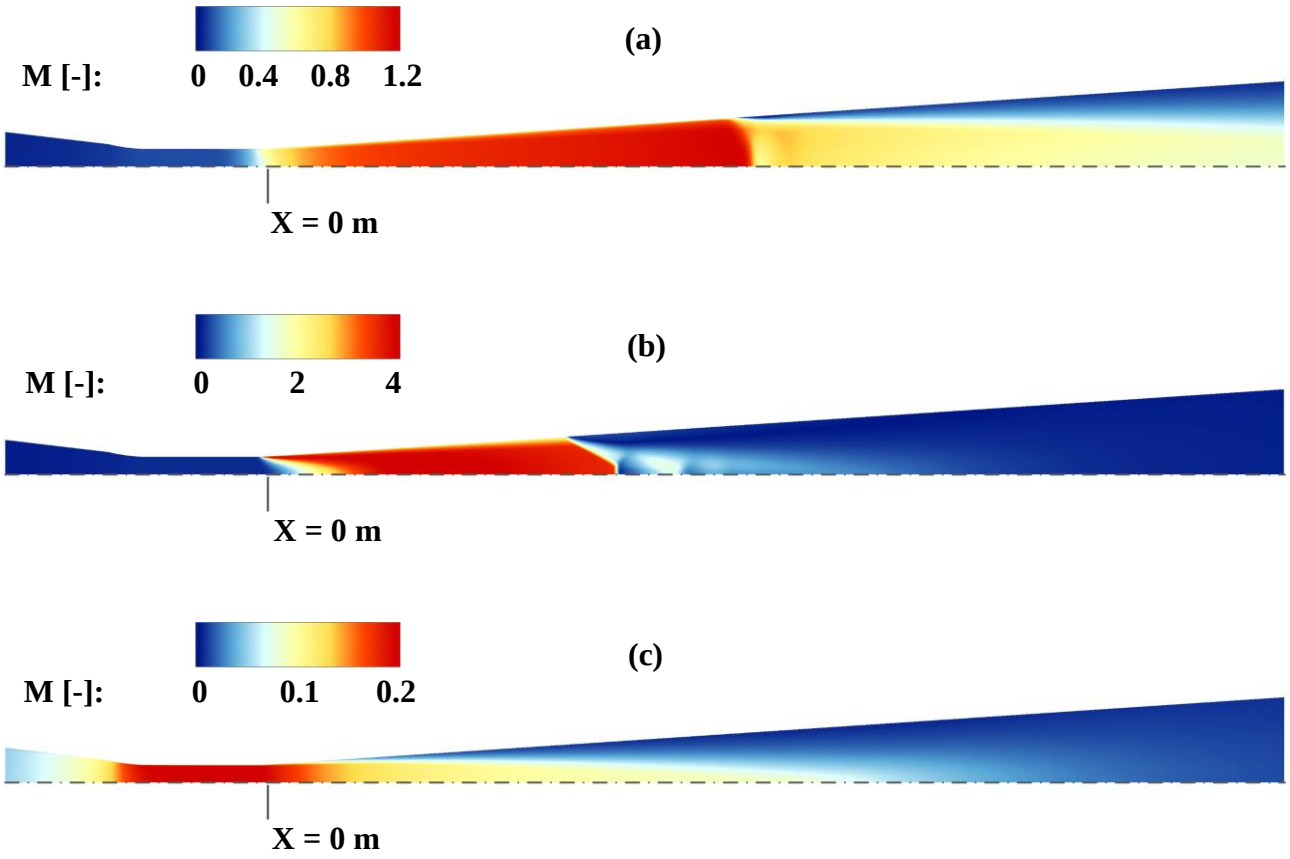

Figure 13. *Contour plot of the Mach number in the throat and downstream regions (predictions of the pressure-based solver): (a) Case 1 of* ***Table*** *: p_{in} / p_{out} = 11.4 bar / 2.6 bar, (b) Case 2 of* ***Table*** *: p_{in} / p_{out} = 43.0 bar / 10.0 bar, and (c) Case 3 of* ***Table*** *: p_{in} / p_{out} = 133.0 bar / 124.2 bar.*

Fig. 14 presents the axial velocity values on four different planes perpendicular to the nozzle axis of symmetry. For the subcritical case 2, **Fig. 14a**, where the flow reaches Mach values up to 4, it is clearly evident that the flow keeps accelerating past the nozzle throat (X = 0.0 m). Hence, the flow expansion due to the compressible nature of the two-phase mixture is once again demonstrated. On the contrary, with regards to the supercritical conditions where the fluid retains liquid-like densities (case 3, **Fig. 14b**), the flow reaches the maximum velocity at the end of the throat and then decelerates steadily, suggesting that any influence of compressibility is absent.

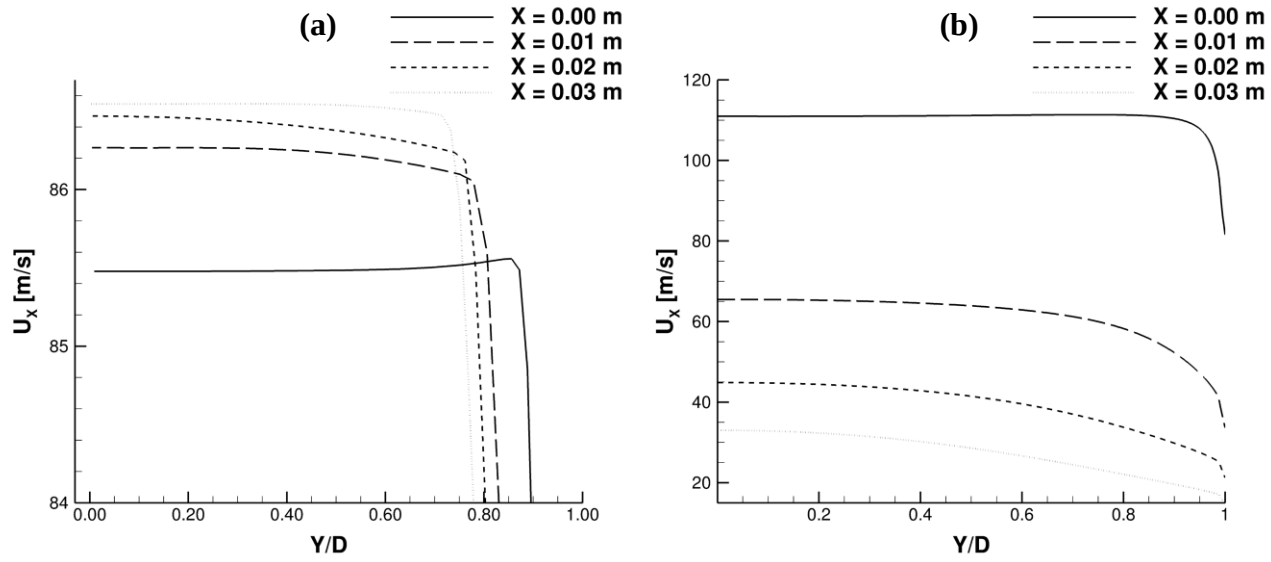

Figure 14. *Cross-flow velocity profiles for: (a) subcritical case 2 ($U_{x,max}$ = 86.6 m/s) and (b) supercritical case 3 ($U_{x,max}$ = 111.4) m/s of* ***Table*** *.*

3.5 Flow instabilities

Flow instabilities arising due to the abrupt changes in pressure and density of the fluid are plausible to influence the flow field in the subcritical regime. In order to fully elucidate such effects, additional DES have been performed for cases 1 and 2 of **Table** . It should be noted that the pressure-based solver was employed in DES with the phase-change rate being imposed through **Eq. (2)**. Average fields were obtained for a total flow time of 5 ms, which is equivalent to 50,000 time steps and are presented in **Fig. 15**.

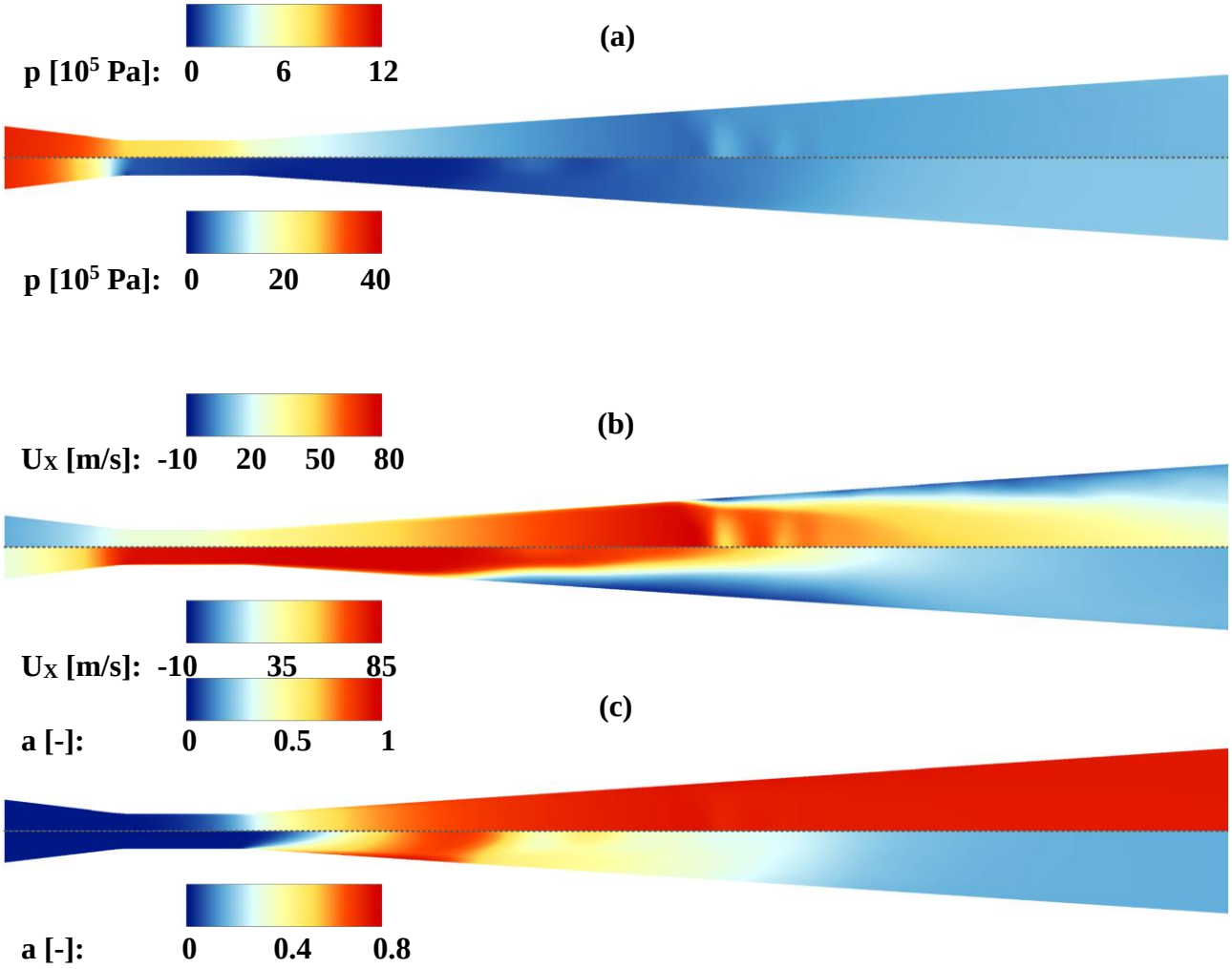

Figure 15. *Contour plots of time-averaged field over the nozzle plane of symmetry; upper frames correspond to case 1 and lower ones to case 2 of* ***Table*** *: (a) pressure (b) axial velocity and (c) vapour-volume fraction. The figures include the part of the nozzle from* $X = -23.5\,mm$ *to* $X = 98.2\,mm$.

The elucidation of the influence of flow instabilities is of high practical importance, since they can affect the delivery performance of the oxidiser injector with subsequent consequences on the combustion efficiency. A recirculation region has been identified immediately downstream of the Mach disk in numerical studies, yet experimental data do not verify this feature [67]. **Fig. 16** depicts three characteristic DES time instances for the subcritical case 2 of **Table** , where a severe jet expansion has been observed; a detailed view of the region slightly downstream the nozzle throat is depicted. The black line evident on the vectors-over-contour plots signifies regions where M=1. The

three instances make clear that the flow is oriented to the direction of the oblique shock-waves and remains parallel in the region encompassed by the M=1 iso-line. On the contrary, as depicted in all three instances a complex recirculation pattern sets in at the subsonic boundary layer. It is also interesting to notice in **Fig. 16a** and **Fig. 16c** that the flow turns away from the nozzle axis, i.e. towards the wall in the flow regions in the vicinity of M=1 iso-lines (annotated as regions 1-3 in the plots). This flow behaviour is also similar to the velocity field of expanding supersonic gas jets [62]. Finally, as shown in **Fig. 16b** significant flow deceleration and transition to the subcritical regime perturbs the flow significantly, so as to induce the emergence of an extensive recirculation pattern even at the channel core (region 4), where parallel flow prevails in the other time instances. As can be observed in the three time instances of **Fig. 16**, the locations in the channel core where the flow decelerates, thus denoting the presence of normal shockwaves, are not fixed in time for case 2. To highlight this behaviour, **Fig. 17** presents the distribution of the pressure gradient over the nozzle symmetry axis for three different time instances. It is evident that the location and the magnitude of the first of the shock cells, which manifests in the vicinity of the axis are not stable but rather oscillating in time, thus producing a less sharp representation on the time-averaged fields, a trend similar to that obtained by the density-based RANS solver, refer to **Fig. 9** and **Fig. 10**. These features have been verified to remain static for the subcritical case 1.

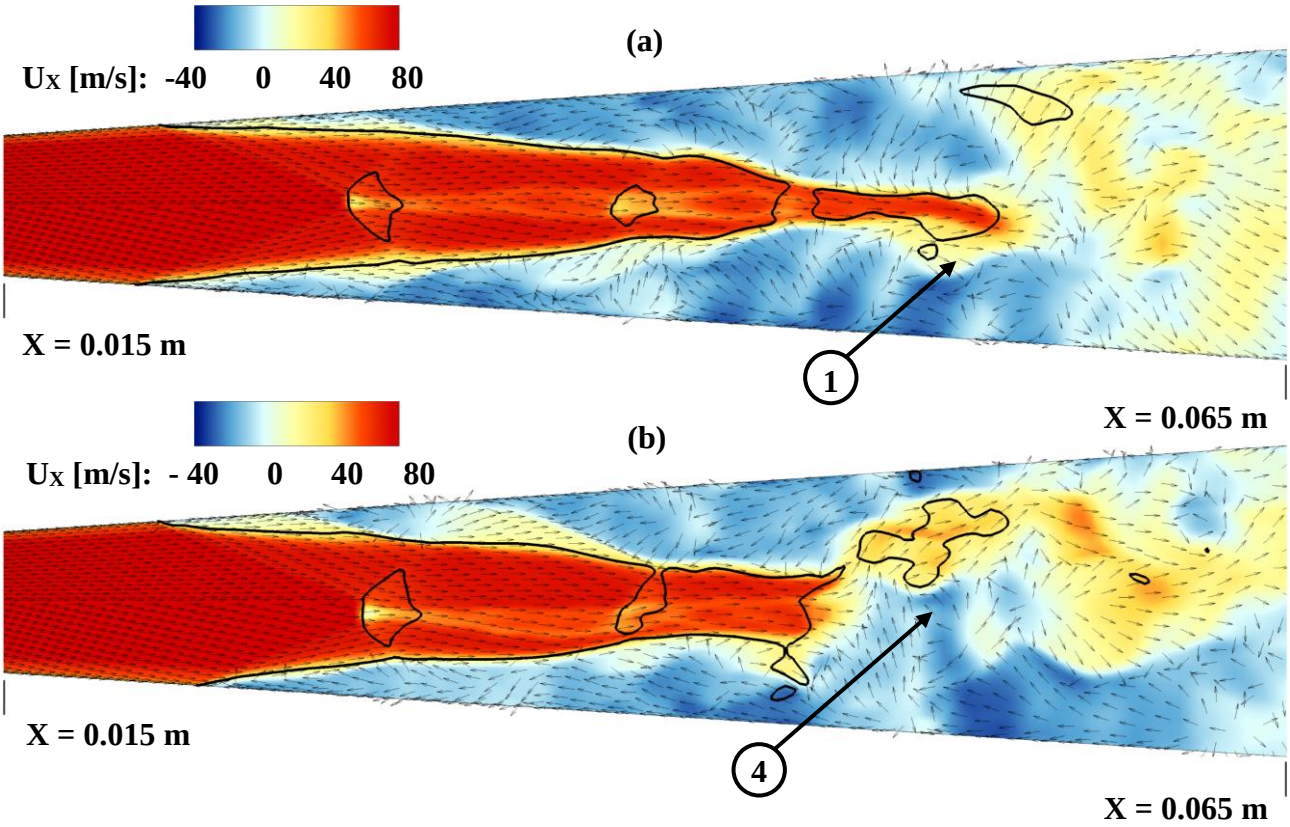

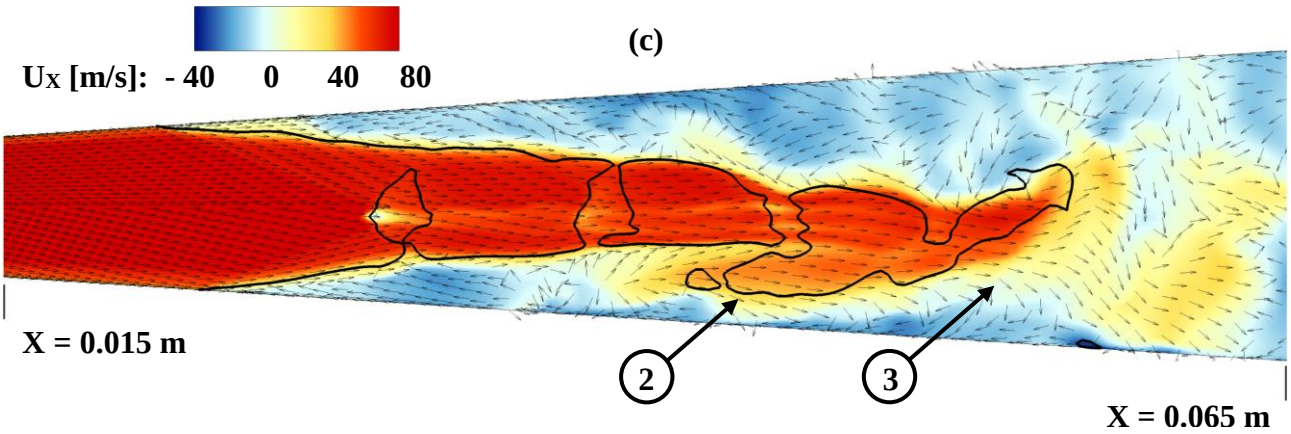

Figure 16: *Velocity vectors over axial velocity contour plots in a detailed view after the nozzle throat exit (X=0.015 m) corresponding to characteristic time instances of DES: (a) t =0.240 s, (b) t+1.0 ms and (c) t+2.0 ms. The black iso-line signifies M=1 regions, while the numbered vectors indicate regions of distinct flow features.*

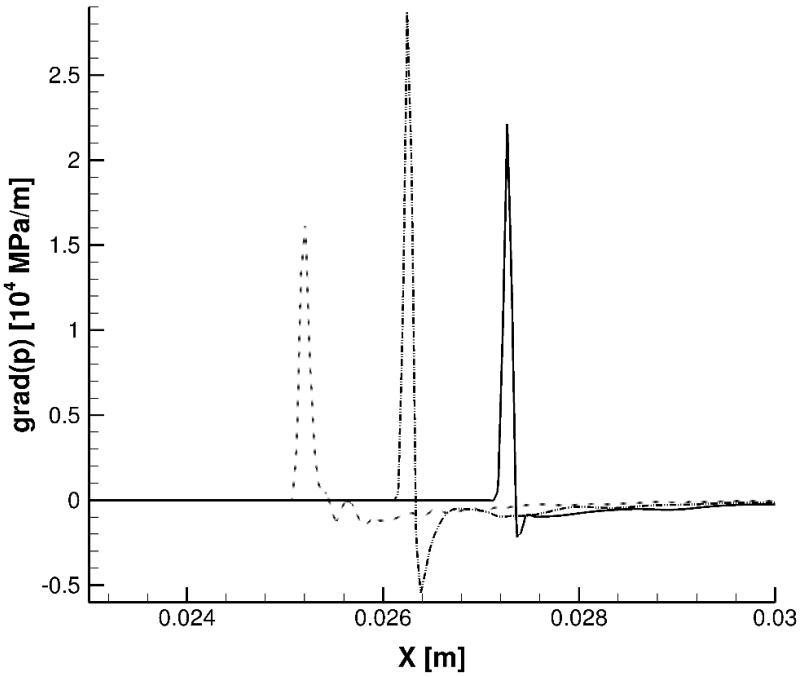

Figure 17. *Distribution of the pressure gradient at the nozzle symmetry axis for case 2 of* ***Table*** *. Time difference between the instances is 0.08 ms.*

In order to highlight the manifestation of turbulence within the nozzle, **Fig. 18** presents a visualization of the vortical structures arising for the subcritical cases 1 and 2, based on the DES results, using Q-criterion iso-surfaces. A common characteristic for both cases, constitutes the almost complete absence of structures in the throat region. Rings are only formed on the walls of the nozzle where the constant-diameter throat begins and ends. A multitude of vortical structures emanating from the shockwave location develop in the diverging section of the nozzle, which, in fact occupy the major part of the section for case 1 (**Fig. 18a**), for which the flow retains high velocities until the outlet, refer to **Fig. 15**. The relevant distribution for case 2 (**Fig. 18b**) exhibits structures of smaller scale densely forming in the region of the shock-diamond system, yet decaying well upstream the nozzle outlet due to the low flow velocities past the normal-shock sequence.

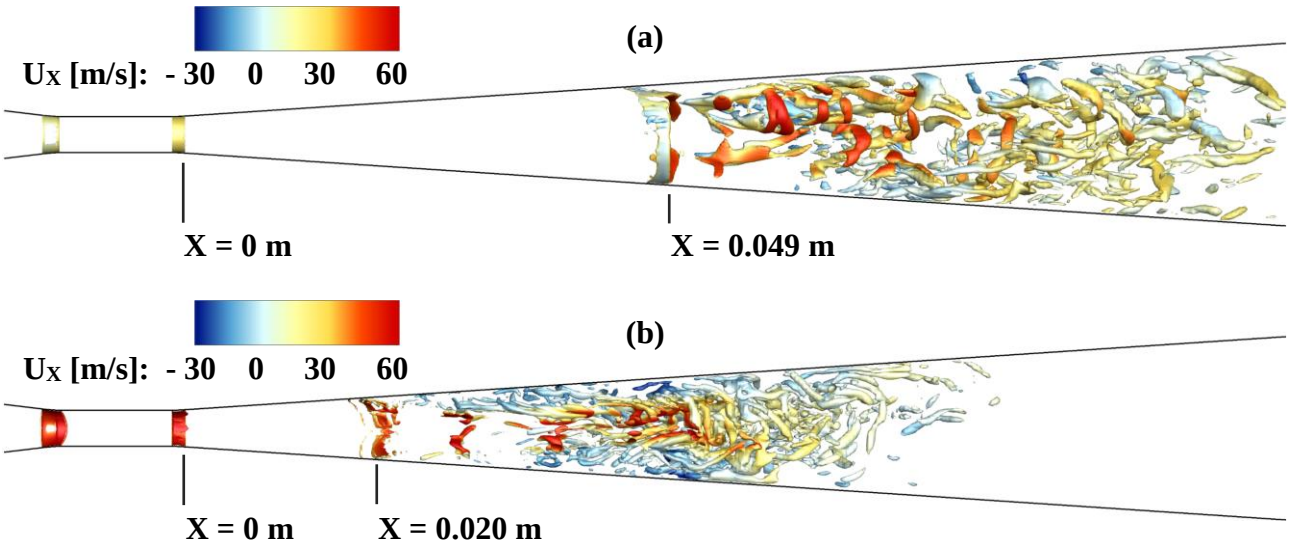

Figure 18. *Visualisation of vortices using Q-Criterion iso-surfaces ($Q=2{\cdot}10^8$) coloured by axial velocity values for the DES results of (a) Case 1 of* ***Table*** *: p_{in} / p_{out} = 11.4 bar / 2.6 bar, (b) Case 2 of* ***Table*** *: p_{in} / p_{out} = 43.0 bar / 10.0 bar. The figures include the part of the nozzle from $X = -0.017\ m$ to $X = 0.11\ m$.*

4. Conclusions

Two-phase oxygen flow was numerically investigated in a converging-diverging nozzle in both sub- and supercritical pressure conditions using both URANS simulations and DES. The selected conditions are typical for the component operation of lower and upper-stage rocket engines. Two phase-change mechanisms have been utilized. A finite phase-change rate imposed by a Hertz-Knudsen-type equation was found to give the most accurate results regarding the two-phase oxygen flow field in the subcritical regime, suggesting a moderate departure from thermodynamic equilibrium. Nevertheless, the tabulated approach based on the Helmholtz EoS proposed in this work was found to produce results of sufficient accuracy for both sub- and supercritical pressure regimes, hence, rendering it a universal modelling approach for cryogenic fluid injection. From a flow physics standpoint, in the supercritical regime the flow exhibits smooth transitions for all quantities of interest. Overall, the flow field exhibits no appreciable distinct features and abrupt gradients. On the contrary, in the subcritical regime, flash boiling of LOx takes place, i.e. abrupt vaporisation of the liquid phase, accompanied by flow acceleration to supersonic velocities and abrupt pressure gradients. In the case with the most severe two-phase jet expansion, a series of shock-diamonds set in at the nozzle diverging region verifying the flow similarity to the expansion of a supersonic gas jet. DES demonstrated that the flow transition from the super- to the subsonic regime perturbs the velocity field and gives rise to extensive recirculation patterns both in the boundary-layer region, as well as in the channel core. The main findings of this study are applicable to propulsion components of space vehicles where LOx is currently the prevalent oxidiser option but also to other applications where cryogenic liquids are the working media, e.g. CO_2 for refrigeration systems.

AKNOWLEDGEMENT

The presented work has received funding from the European Union Horizon 2020 Research and Innovation programme as part of the "Holistic Approach of Spray Injection through a Generalized Multi-phase Framework (HAoS)" project. Grant Agreement ID: 675676.

References

[1] K. Harstad and J. Bellan, "Interactions of fluid oxygen drops in fluid hydrogen at rocket chamber pressures," *International Journal of Heat and Mass Transfer*, vol. 41, no. 22, pp. 3551–3558, 1998, doi: 10.1016/S0017-9310(98)00048-9.

[2] V. Yang, "Liquid-Propellant Rocket Engine Injector Dynamics and Combustion Processes at Supercritical Conditions:," Defense Technical Information Center, Fort Belvoir, VA, 2004. doi: 10.21236/ADA428947.

[3] D. Coulon, "Vulcain-2 Cryogenic Engine Passes First Test with New Nozzle Extension," *ESA Bouletin*, vol. 102, pp. 123–124, 2000.

[4] S. R. Shine, S. Sunil Kumar, and B. N. Suresh, "A new generalised model for liquid film cooling in rocket combustion chambers," *International Journal of Heat and Mass Transfer*, vol. 55, no. 19–20, pp. 5065–5075, 2012, doi: 10.1016/j.ijheatmasstransfer.2012.05.006.

[5] H. Meng and V. Yang, "Vaporization of two liquid oxygen (LOX) droplets in tandem in convective hydrogen streams at supercritical pressures," *International Journal of Heat and Mass Transfer*, vol. 68, pp. 500–508, 2014, doi: 10.1016/j.ijheatmasstransfer.2013.09.041.

[6] R. Ingebo, "Cryogenic spray vaporization in high-velocity helium, argon and nitrogen gasflows," presented at the 32nd Aerospace Sciences Meeting and Exhibit, Reno, NV, U.S.A., 1994, doi: 10.2514/6.1994-687.

[7] J. R. Simões-Moreira and C. W. Bullard, "Pressure drop and flashing mechanisms in refrigerant expansion devices," *International Journal of Refrigeration*, vol. 26, no. 7, pp. 840–848, 2003, doi: 10.1016/S0140-7007(03)00070-7.

[8] H. Guo, B. Wang, Y. Li, H. Xu, and Z. Wu, "Characterizing external flashing jet from single-hole GDI injector," *International Journal of Heat and Mass Transfer*, vol. 121, pp. 924–932, 2018, doi: 10.1016/j.ijheatmasstransfer.2018.01.042.

[9] M. Habiballah, M. Orain, F. Grisch, L. Vingert, and P. Gicquel, "Experimental Studies of High-Pressure Cryogenic Flames on the Mascotte Facility," *Combustion Science and Technology*, vol. 178, no. 1–3, pp. 101–128, 2006, doi: 10.1080/00102200500294486.

[10] R. C. Hendricks, R. J. Simoneau, and R. F. Barrows, "Two-phase choked flow of subcooled oxygen and nitrogen," *STIN 18376*, 1976.

[11] W. Mayer and H. Tamura, "Propellant injection in a liquid oxygen/gaseous hydrogen rocket engine," *Journal of Propulsion and Power*, vol. 12, no. 6, pp. 1137–1147, 1996, doi: 10.2514/3.24154.

[12] W. O. H. Mayer *et al.*, "Atomization and Breakup of Cryogenic Propellants Under High-Pressure Subcritical and Supercritical Conditions," *Journal of Propulsion and Power*, vol. 14, no. 5, pp. 835–842, Sep. 1998, doi: 10.2514/2.5348.

[13] L. Vingert, G. Ordonneau, N. Fdida, and P. Grenard, “A Rocket Engine under a Magnifying Glass,” *AerospaceLab Journal*, vol. Issue 11, p. 13 pages, 2016, doi: 10.12762/2016.AL11-15.

[14] B. Chehroudi, D. Talley, and E. Coy, “Visual characteristics and initial growth rates of round cryogenic jets at subcritical and supercritical pressures,” *Physics of Fluids*, vol. 14, no. 2, pp. 850–861, 2002, doi: 10.1063/1.1430735.

[15] G. Lamanna *et al.*, “Flashing Behavior of Rocket Engine Propellants,” *Atomization and Sprays*, vol. 25, no. 10, pp. 837–856, 2015, doi: 10.1615/AtomizSpr.2015010398.

[16] G. Lamanna, H. Kamoun, B. Weigand, and J. Steelant, “Towards a unified treatment of fully flashing sprays,” *International Journal of Multiphase Flow*, vol. 58, pp. 168–184, 2014, doi: 10.1016/j.ijmultiphaseflow.2013.08.010.

[17] S. Yamamoto and T. Furusawa, “Thermophysical flow simulations of rapid expansion of supercritical solutions (RESS),” *The Journal of Supercritical Fluids*, vol. 97, pp. 192–201, 2015, doi: 10.1016/j.supflu.2014.11.016.

[18] Z. Yuan, W. Yangle, C. Jingtan, X. Zhaoyang, and W. Junfeng, “Numerical Simulation of Supercritical Carbon Dioxide Critical Flow in the Nozzle Tube,” *Journal of Nuclear Engineering and Radiation Science*, vol. 4, no. 1, p. 011018, 2018, doi: 10.1115/1.4037896.

[19] Z. Zhou, Y. Lu, J. Tang, X. Zhang, and Q. Li, “Numerical simulation of supercritical carbon dioxide jet at well bottom,” *Applied Thermal Engineering*, vol. 121, pp. 210–217, 2017, doi: 10.1016/j.applthermaleng.2017.04.060.

[20] K. Chen, R.-N. Xu, and P.-X. Jiang, “Numerical investigation of jet impingement cooling of a low thermal conductivity plate by supercritical pressure carbon dioxide,” *International Journal of Heat and Mass Transfer*, vol. 124, pp. 1003–1010, 2018, doi: 10.1016/j.ijheatmasstransfer.2018.04.003.

[21] S. K. Raman and H. D. Kim, “Solutions of supercritical CO2 flow through a convergent-divergent nozzle with real gas effects,” *International Journal of Heat and Mass Transfer*, vol. 116, pp. 127–135, 2018, doi: 10.1016/j.ijheatmasstransfer.2017.09.019.

[22] H. Müller, C. A. Niedermeier, J. Matheis, M. Pfitzner, and S. Hickel, “Large-eddy simulation of nitrogen injection at trans- and supercritical conditions,” *Physics of Fluids*, vol. 28, no. 1, p. 015102, 2016, doi: 10.1063/1.4937948.

[23] A. Poormahmood, M. Shahsavari, and M. Farshchi, “Numerical Study of Cryogenic Swirl Injection Under Supercritical Conditions,” *Journal of Propulsion and Power*, vol. 34, no. 2, pp. 428–437, 2018, doi: 10.2514/1.B36569.

[24] J. Kang, J. Heo, H.-G. Sung, and Y. Yoon, “Dynamic characteristics of a cryogenic nitrogen swirl injector under supercritical conditions,” *Aerospace Science and Technology*, vol. 67, pp. 398–411, 2017, doi: 10.1016/j.ast.2017.04.010.

[25] N. Zong and V. Yang, “Cryogenic fluid dynamics of pressure swirl injectors at supercritical conditions,” *Physics of Fluids*, vol. 20, no. 5, p. 056103, 2008, doi: 10.1063/1.2905287.

[26] X. Wang, H. Huo, Y. Wang, L. Zhang, and V. Yang, “A Three-Dimensional Analysis of Swirl Injector Flow Dynamics at Supercritical Conditions,” presented at the 53rd AIAA Aerospace Sciences Meeting, Kissimmee, Florida, 2015, doi: 10.2514/6.2015-1827.

[27] X. Wang, H. Huo, Y. Wang, and V. Yang, "Comprehensive Study of Cryogenic Fluid Dynamics of Swirl Injectors at Supercritical Conditions," *AIAA Journal*, vol. 55, no. 9, pp. 3109–3119, 2017, doi: 10.2514/1.J055868.

[28] E. Sher, T. Bar-Kohany, and A. Rashkovan, "Flash-boiling atomization," *Progress in Energy and Combustion Science*, vol. 34, no. 4, pp. 417–439, 2008, doi: 10.1016/j.pecs.2007.05.001.

[29] J. R. Travis, D. Piccioni Koch, and W. Breitung, "A homogeneous non-equilibrium two-phase critical flow model," *International Journal of Hydrogen Energy*, vol. 37, no. 22, pp. 17373–17379, 2012, doi: 10.1016/j.ijhydene.2012.07.077.

[30] K. Lyras, S. Dembele, D. P. Schmidt, and J. X. Wen, "Numerical simulation of subcooled and superheated jets under thermodynamic non-equilibrium," *International Journal of Multiphase Flow*, vol. 102, pp. 16–28, 2018, doi: 10.1016/j.ijmultiphaseflow.2018.01.014.

[31] R. Schmehl and J. Steelant, "Computational Analysis of the Oxidizer Preflow in an Upper-Stage Rocket Engine," *Journal of Propulsion and Power*, vol. 25, no. 3, pp. 771–782, 2009, doi: 10.2514/1.38309.

[32] T. Ramcke, A. Lampmann, and M. Pfitzner, "Simulations of Injection of Liquid Oxygen/Gaseous Methane Under Flashing Conditions," *Journal of Propulsion and Power*, vol. 34, no. 2, pp. 395–407, 2018, doi: 10.2514/1.B36412.

[33] P. Gaillard, C. L. Touze, L. Matuszewski, and A. Murrone, "Numerical Simulation of Cryogenic Injection in Rocket Engine Combustion Chambers," no. 11, p. 15, 2016.

[34] B. Abramzon and W. A. Sirignano, "Droplet vaporization model for spray combustion calculations," *International Journal of Heat and Mass Transfer*, vol. 32, no. 9, pp. 1605–1618, 1989, doi: 10.1016/0017-9310(89)90043-4.

[35] P. Koukouvinis, A. Vidal-Roncero, C. Rodriguez, M. Gavaises, and L. Pickett, "High pressure/high temperature multiphase simulations of dodecane injection to nitrogen: Application on ECN Spray-A," *Fuel*, vol. 275, p. 117871, 2020, doi: 10.1016/j.fuel.2020.117871.

[36] A. Vidal, K. Kolovos, M. R. Gold, R. J. Pearson, P. Koukouvinis, and M. Gavaises, "Preferential cavitation and friction-induced heating of multi-component Diesel fuel surrogates up to 450MPa," *International Journal of Heat and Mass Transfer*, vol. 166, p. 120744, 2021, doi: 10.1016/j.ijheatmasstransfer.2020.120744.

[37] I. K. Karathanassis, P. Koukouvinis, and M. Gavaises, "Comparative evaluation of phase-change mechanisms for the prediction of flashing flows," *International Journal of Multiphase Flow*, vol. 95, pp. 257–270, 2017, doi: 10.1016/j.ijmultiphaseflow.2017.06.006.

[38] N. Kyriazis, P. Koukouvinis, and M. Gavaises, "Numerical investigation of bubble dynamics using tabulated data," *International Journal of Multiphase Flow*, vol. 93, pp. 158–177, 2017, doi: 10.1016/j.ijmultiphaseflow.2017.04.004.

[39] N. Kyriazis, P. Koukouvinis, I. Karathanassis, and M. Gavaises, "A Tabulated Data Technique For Cryogenic Two-Phase Flows," presented at the ECCM 6, ECFD 7, Glasgow, UK, 2018.

[40] D. Fuster, G. Hauke, and C. Dopazo, "Influence of the accommodation coefficient on nonlinear bubble oscillations," *The Journal of the Acoustical Society of America*, vol. 128, no. 1, pp. 5–10, 2010, doi: 10.1121/1.3436520.

[41] C. E. Brennen, *Cavitation and bubble dynamics*. New York: Cambridge University Press, 2014.

[42] B. M. Devassy, D. Benković, Z. Petranovic, W. Edelbauer, and M. Vujanovic, "Numerical Simulation of Internal Flashing in a GDI Injector Nozzle," presented at the ILASS–Europe, Paris, France, 2019.

[43] R. Schmidt and W. Wagner, "A new form of the equation of state for pure substances and its application to oxygen," *Fluid Phase Equilibria*, vol. 19, no. 3, pp. 175–200, 1985, doi: 10.1016/0378-3812(85)87016-3.

[44] R. B. Stewart, R. T. Jacobsen, and W. Wagner, "Thermodynamic Properties of Oxygen from the Triple Point to 300 K with Pressures to 80 MPa," *Journal of Physical and Chemical Reference Data*, vol. 20, no. 5, pp. 917–1021, 1991, doi: 10.1063/1.555897.

[45] E. W. Lemmon and R. T. Jacobsen, "Viscosity and Thermal Conductivity Equations for Nitrogen, Oxygen, Argon, and Air," *International Journal of Thermophysics*, vol. 25, no. 1, pp. 21–69, 2004, doi: 10.1023/B:IJOT.0000022327.04529.f3.

[46] S. Schmidt, I. Sezal, G. Schnerr, and M. Talhamer, "Riemann Techniques for the Simulation of Compressible Liquid Flows with Phase-Transistion at all Mach Numbers - Shock and Wave Dynamics in Cavitating 3-D Micro and Macro Systems," presented at the 46th AIAA Aerospace Sciences Meeting and Exhibit, Reno, Nevada, 2008, doi: 10.2514/6.2008-1238.

[47] M.-S. Liou, "A sequel to AUSM, Part II: AUSM+-up for all speeds," *Journal of Computational Physics*, vol. 214, no. 1, pp. 137–170, 2006, doi: 10.1016/j.jcp.2005.09.020.

[48] E. F. Toro, *Riemann Solvers and Numerical Methods for Fluid Dynamics: A Practical Introduction*. Springer Berlin Heidelberg, 2013.

[49] E. W. Lemmon and R. Tillner-Roth, "A Helmholtz energy equation of state for calculating the thermodynamic properties of fluid mixtures," *Fluid Phase Equilibria*, vol. 165, no. 1, pp. 1–21, 1999, doi: 10.1016/S0378-3812(99)00262-9.

[50] M. Dumbser, U. Iben, and C.-D. Munz, "Efficient implementation of high order unstructured WENO schemes for cavitating flows," *Computers & Fluids*, vol. 86, pp. 141–168, 2013, doi: 10.1016/j.compfluid.2013.07.011.

[51] F. R. Menter, "Two-equation eddy-viscosity turbulence models for engineering applications," *AIAA Journal*, vol. 32, no. 8, pp. 1598–1605, 1994, doi: 10.2514/3.12149.

[52] M. L. Shur, P. R. Spalart, M. Kh. Strelets, and A. K. Travin, "A hybrid RANS-LES approach with delayed-DES and wall-modelled LES capabilities," *International Journal of Heat and Fluid Flow*, vol. 29, no. 6, pp. 1638–1649, 2008, doi: 10.1016/j.ijheatfluidflow.2008.07.001.

[53] F. R. Menter and M. Kuntz, "Adaptation of Eddy-Viscosity Turbulence Models to Unsteady Separated Flow Behind Vehicles," in *The Aerodynamics of Heavy Vehicles: Trucks, Buses, and Trains*, vol. 19, R. McCallen, F. Browand, and J. Ross, Eds. Berlin, Heidelberg: Springer Berlin Heidelberg, 2004, pp. 339–352.

[54] S. J. Sherwin and H. M. Blackburn, "Three-dimensional instabilities and transition of steady and pulsatile axisymmetric stenotic flows," *J. Fluid Mech.*, vol. 533, 2005, doi: 10.1017/S0022112005004271.

[55] P. Brossel, S. Eury, P. Signol, H. Laporte-Weywada, and J. Micewicz, “Development status of the Vulcain engine,” presented at the 31st Joint Propulsion Conference and Exhibit, San Diego,CA,U.S.A., 1995, doi: 10.2514/6.1995-2539.

[56] A. Arnone, P. Boncinelli, A. Munari, and E. Spano, “Application of CFD techniques to the design of the Ariane 5 turbopump,” presented at the 14th Computational Fluid Dynamics Conference, Norfolk,VA,U.S.A., 1999, doi: 10.2514/6.1999-3380.

[57] N. Kyriazis, P. Koukouvinis, and M. Gavaises, “Modelling cavitation during drop impact on solid surfaces,” *Advances in Colloid and Interface Science*, vol. 260, pp. 46–64, 2018, doi: 10.1016/j.cis.2018.08.004.

[58] W. Mayer, J. Telaar, R. Branam, G. Schneider, and J. Hussong, “Raman Measurements of Cryogenic Injection at Supercritical Pressure,” *Heat and Mass Transfer*, vol. 39, no. 8–9, pp. 709–719, 2003, doi: 10.1007/s00231-002-0315-x.

[59] Md. Alamgir and J. H. Lienhard, “Correlation of Pressure Undershoot During Hot-Water Depressurization,” *Journal of Heat Transfer*, vol. 103, no. 1, pp. 52–55, 1981, doi: 10.1115/1.3244429.

[60] V. N. Blinkov, O. C. Jones, and B. I. Nigmatulin, “Nucleation and flashing in nozzles—2. Comparison with experiments using a five-equation model for vapor void development,” *International Journal of Multiphase Flow*, vol. 19, no. 6, pp. 965–986, 1993, doi: 10.1016/0301-9322(93)90072-3.

[61] P. Downar-Zapolski, Z. Bilicki, L. Bolle, and J. Franco, “The non-equilibrium relaxation model for one-dimensional flashing liquid flow,” *International Journal of Multiphase Flow*, vol. 22, no. 3, pp. 473–483, 1996, doi: 10.1016/0301-9322(95)00078-X.

[62] A. Hamzehloo and P. G. Aleiferis, “LES and RANS modelling of under-expanded jets with application to gaseous fuel direct injection for advanced propulsion systems,” *International Journal of Heat and Fluid Flow*, vol. 76, pp. 309–334, 2019, doi: 10.1016/j.ijheatfluidflow.2019.01.017.

[63] T. C. Adamson and J. A. Nicholls, “On the Structure of Jets from Highly Underexpanded Nozzles Into Still Air,” *Journal of the Aerospace Sciences*, vol. 26, no. 1, pp. 16–24, 1959, doi: 10.2514/8.7912.

[64] S. Crist, D. R. Glass, and P. M. Sherman, “Study of the highly underexpanded sonic jet.,” *AIAA Journal*, vol. 4, no. 1, pp. 68–71, 1966, doi: 10.2514/3.3386.

[65] V. Vuorinen, J. Yu, S. Tirunagari, O. Kaario, and M. Larmi, “Large-eddy simulation of highly underexpanded transient gas jets,” *Physics of Fluids*, vol. 25, p. 23, 2013, doi: doi: 10.1063/1.4772192.

[66] E. Franquet, V. Perrier, S. Gibout, and P. Bruel, “Free underexpanded jets in a quiescent medium_ A review,” *Progress in Aerospace Sciences*, p. 29, 2015, doi: https://doi.org/10.1016/j.paerosci.2015.06.006.

[67] D. Edgington-Mitchell, D. R. Honnery, and J. Soria, “The underexpanded jet Mach disk and its associated shear layer,” *Physics of Fluids*, vol. 26, no. 9, p. 096101, 2014, doi: 10.1063/1.4894741.